

Optimizing Quantum Photonic Integrated Circuits using Differentiable Tensor Networks

Mathias Van Regemortel and Thomas Van Vaerenbergh

Large-Scale Integrated Photonics Lab, Hewlett Packard Labs, HPE Belgium, Diegem, Belgium

Recent reports of large photonic nonlinearities in integrated photonic devices, using the strong excitonic light-matter coupling in semiconductors, necessitate a tailored design framework for quantum processing in the limit of low photon occupation. We present a gradient-based optimization method for quantum photonic integrated circuits, which are composed of nonlinear unitary coupling gates and stochastic, nonunitary components for sampling the photonic losses. As core of our method, differentiable tensor-networks are leveraged, which are accurate in the regime of low photonic occupation and modest intermode entanglement. After characterizing the circuit gate architecture with field simulations of GaAs-based samples, we demonstrate the applicability of our method by optimizing quantum photonic circuits for two key use cases: integrated designs for quantum optical state preparation and tailored optimal readout for quantum phase sensing.

1 Introduction

Recent experiments reported that optical nonlinearities can be impressively enhanced with external electric fields [1, 2, 3], opening the way to quantum processing using the strong light-matter excitonic coupling in semiconductor samples [4, 5]. Planar samples, provide, on one side, the flexibility for etching optical gate architectures in 2D topologies and, on the other, the near-infrared wavelength compatibility that aligns with existing fiber-optic infrastructures. This opens up a pathway for integrating semiconductor quantum processing platforms into state-of-the-art channels for communication and sensing.

Mathias Van Regemortel: mathias.van-regemortel@hpe.com

When harnessed appropriately, the non-classical photonic statistics may outperform the classical counterpart in both computing, as well as, sensing applications, as was recently shown for several experimental test cases, such as Gaussian boson sampling [6] and photonic quantum sensing and metrology [7, 8, 9]. This transition into quantum regimes is achieved through various mechanisms, such as optical parametric oscillation (OPO) [10, 11], exciton-mediated Kerr-type nonlinearities [12, 13], and even full photon blockade [14] — each offering distinct avenues for accessing and controlling strongly non-classical states of light.

While numerous optimization frameworks have been developed and benchmarked for the design of classical linear photonic integrated circuits (PICs) to perform tasks in the domain of optical computation [15, 16, 17, 18, 19, 20] and machine learning [21], the systematic capture of relevant statistics for quantum processing in quantum PICs (qPICs) remains largely unexplored. The coherent Poissonian photon statistics, at the heart of linear optics, is broken by the presence of optical Kerr-type nonlinearities, thus enabling the generation of light with strong non-classical photon statistics, beyond the amplitude-phase representation of classical coherent laser light. Instead, the description of the photonic quantum state must be explicitly integrated in the qPIC optimization scheme, which can be achieved by, either, a truncated, but exponentially growing bosonic Hilbert space, a suitable variational ansatz, or phase-space sampling methods [22].

In this work, we present a gradient-based variational optimization method for qPICs, based on differentiable tensor contractions within a matrix product state (MPS) representation of the multimode bosonic photon state, where each mode is described by a truncated local Fock space. Two key features underpin the suitability of the

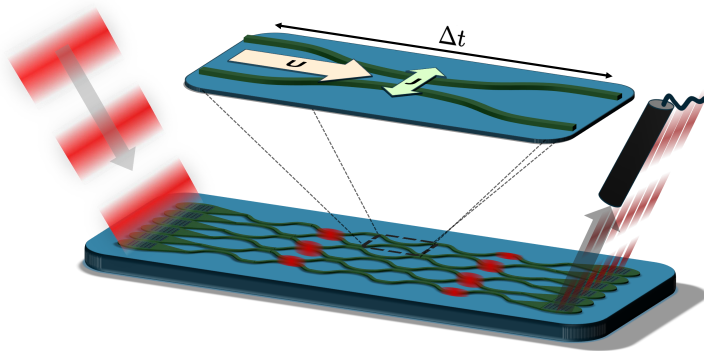


Figure 1: The optical circuits used for quantum optimization. A pulsed coherent laser light is coupled into the integrated waveguides and propagates through a bricked pattern of optical nonlinear gates. After the nonlinear quantum processing in the optical chip, the output light is detected for analysis and optimization. The inset illustrates the gate design in more detail; it consists of a linear coupling rate J between two adjacent waveguides, a photonic Kerr-nonlinearity U , constant throughout, and a gate propagation time Δt . The couplings J are iteratively adjusted by simulating the optical quantum circuit and minimizing a figure of merit defined on the output light.

method for quantum photonic optimization in this context: (i) the modest, area-law entanglement characteristic of these quantum states can be controllably captured using the matrix product state (MPS) formalism [23], and (ii) stochastic waveguide losses can be incorporated via Monte Carlo trajectory sampling [24, 25, 26] in the MPS formalism [27, 28], while maintaining the differentiability of tensor operations. This is essential for gradient-based optimization. Next, we demonstrate the possibilities of the proposed optimization method through two key applications in the regime of low photon occupation: (i) the design of optimal qPICs for quantum state preparation and (ii) the achieving of optimal readout for quantum phase sensing.

Contributions The design of the qPIC is illustrated on Fig. 1; for the optimization the start is to define a figure of merit (FOM) $\mathcal{L}[|\psi_{\text{out}}\rangle]$ on the qPIC output state $|\psi_{\text{out}}\rangle$ for executing the optimization of the targeted quantum processing task. Considering injection of coherent laser pulses into the circuit, the nonclassical circuit output state depends explicitly on the circuit gate couplers, $|\psi_{\text{out}}(\{J_{l,d}\})\rangle$, with $\{J_{l,d}\}$ the coupling rate of gate l in circuit layer d , which couple the waveguides l and $l + 1$. The final objective of the optimization is to obtain a set of optimal couplers,

$$\{J_{l,d}^{(\text{opt})}\} := \text{argmin}_{\{J_{l,d}\}} \mathcal{L}[|\psi_{\text{out}}(\{J_{l,d}\})\rangle]. \quad (1)$$

For a given waveguide etch depth on the semiconductor chip, the couplings $J_{l,d}$ can be controlled in the fabrication by varying the coupler separation and length [29, 30].

In this work, we contribute to the development of qPIC-based quantum processing in the following ways,

1. A framework for solidifying the circuit gate description and parametrization is presented, based on 2D field simulations of GaAs etched samples – see Sec. 2 for a summary and Appendices A-B for the details of the simulations.
2. The development of a differentiable optical tensor framework for qPIC simulation and optimization. While similar methods for quantum optimization were presented before in Ref. [31], we developed our own code repository, specifically tailored for (i) photonic (bosonic) quantum simulation and optimization, (ii) optimization within the manifold of Kerr nonlinear coupling gates, (iii) the inclusion of photonic noise channels using stochastic sampling, and (iv) addressing specific photonic optimization tasks. It is publicly available in Ref. [32] – see Sec. 3.
3. Establishing qPIC designs for quantum state generation. Here, we focus on deep-circuit cat-state generation and noisy single-photon sampling, with inclusion of photonic losses – see Sec. 4.

4. Optimizing a qPIC design for quantum phase-sensing readout from coherent input light – see Sec. 5.

2 The gate design and circuit dynamics from field equations

As an experimental baseline for implementing the design of the qPIC, we focus on GaAs-based planar heterostructures, which have an exciton resonance close to 780 nm that mediates the photonic nonlinearity in the strong light-matter coupling regime. The qPIC consists of layers of stacked nonlinear coupling gates, as is illustrated on Fig. 1.

Each two mode coupler is defined by an effective coupling Hamiltonian of the form,

$$H^{(2)}(J, U) = -\hbar J (a_1^\dagger a_2 + a_2^\dagger a_1) + \frac{\hbar U}{2} (a_1^{\dagger 2} a_1^2 + a_2^{\dagger 2} a_2^2), \quad (2)$$

where J describes the tunneling rate, per time, and U the intra-waveguide nonlinearity photons are exposed to, also expressed as a rate (inverse time). When the Hamiltonian (2) is applied for some time Δt to the photonic field (the time for photons to transfer through the gate) we retrieve unitary gates of the following form,

$$V(J, U; \Delta t) = e^{-i\Delta t H^{(2)}(J, U)}, \quad (3)$$

which are fully characterized by a set of two dimensionless parameters, $(J\Delta t, U\Delta t)$.

We consider qPIC designs etched on GaAs-based chips using standard fabrication techniques (see, e.g., Ref. [33]) to shape an effective transverse confinement potential for the photonic field. In Appendix A, we run 2D field simulations of a nonlinear coupler etched on a planar GaAs sample, excited with a pulsed laser, using realistic experimental parameters. The goal is to identify the parameters (J, U) , from Eq. (2), that characterize the circuit gates. Next, starting from the 2D field simulations, an effective model of 1D coupled ordinary differential equations (ODEs) can be derived to describe a coupled set of waveguides with coupling parameter J . These are subsequently used for gauging the circuit gate parameters $(U, \Delta t)$, considering pulsed laser excitation, close to the exciton resonance. The photons enclosed in one laser pulse in waveguide l can be considered a single bosonic mode a_l , in case the

spatial extent of the pulse is well-contained, below the polaritonic coherence length. This we verify in Appendix B by comparing the photon pulse field dynamics in the waveguide with an effective reduced circuit gate model for the bosonic operator a_l .

We give a short overview of the material and pulse parameters that influence the gates.

- **The exciton interaction constant:** The planar GaAs quantum well induces a photonic nonlinearity g_{2D} due to the strong coupling to the interacting excitons [34]. The strength of this interaction sets, for a large part, the effective nonlinearity experienced by the bosonic modes in the circuit representation. Reported values range from $g_{2D} = 6 - 10 \mu\text{eV} \mu\text{m}^2$ in unperturbed samples [35, 2], while applying an electric field gives nonlinearities up to $g_{2D} = 600 \mu\text{eV} \mu\text{m}^2$, as reported in Ref. [3].
- **Polariton group velocity:** the group velocity of the polaritons is determined by their coupling to the exciton field, set by the wavelength and in-plane wavevector of the light. Values of $v_g = 26 \mu\text{m ps}^{-1}$ have been reported in literature [36]. This will, on the one hand, impact Δt and, on the other, the spatial extent of the pulse in the sample. More compressed pulses generate higher nonlinearity, as can be seen from,

$$U = \int_{\mathcal{S}} d^2r n(\mathbf{r}) [g_{2D} n(\mathbf{r})], \quad (4)$$

with $n(\mathbf{r})$ the normalized photon field density of the pulse in the semiconductor plane \mathcal{S} , confined in the transverse magnetic zero eigenmode of the waveguide (TM₀-mode) for maximal coupling [37], and $g_{2D} n(\mathbf{r})$ the nonlinear energy shift at point \mathbf{r} . Thus, lowering v_g amounts to an enhanced effective gate nonlinearity due to an increase in exposure time. This can be achieved at higher exciton fraction or with methods of slow light [38].

- **Excitonic fraction of polariton field:** By varying the light frequency and in-plane wavevector, the exciton fraction of the polariton mode, $a_{\text{LP}}(\mathbf{k}) = u_k a_{\text{ph}}(\mathbf{k}) + v_k a_{\text{ex}}(\mathbf{k})$, with $u_k^2 + v_k^2 = 1$, can be scanned with the laser detuning from the exciton resonance, given by v_k^2 . Higher exciton fraction gives

slower propagation (the exciton is largely immobile as compared to the photons) and higher nonlinearity.

- **Etched waveguide separation:** The photonic tunneling rate from one waveguide to the other is, to first order, determined by the overlap between the two transverse waveguide eigenmodes [29]. We assume a conservative separation between the waveguides of the order of ~ 500 nm [33].

After analysis in Appendices A and B, we find that a reasonable parameter range for GaAs gates, with a gate length of the order of $100\mu\text{m}$, are $0 \leq J\Delta t \leq \pi$, maximally a full tunneling rotation between the waveguides, and $0 \leq U\Delta t \leq 0.25$. This is what we will use as a baseline for developing the circuit tensor-based gradient-descent optimization scheme.

3 Tensor network circuit optimization

Having established the architecture of nonlinear optical gates with coupling rates as optimization variables that can be determined during the chip-design phase, we now introduce the differentiable tensor network framework for dissipative quantum circuits that allows to find the optimal values of these coupling rates. This approach is valid in the low-photon regime, due to the explicit single-mode bosonic Fock-space truncation, with limited intermode entanglement.

In Sec. 3.1, we describe the tensor network contraction of the optical circuit using the MPS representation of multimode photonic states. In Sec. 3.2, we extend this representation with a batch index to enable stochastic sampling of dissipation via non-unitary gates. Finally, Sec. 3.3 details the gradient-based optimization scheme using the tensor network representation of the qPIC.

3.1 The tensor-network photonic circuit contraction

The full circuit consists of L parallel waveguides, on which two-mode nonlinear coupling gates are organized in a bricked pattern of depth D – see Fig. 2. Each two-mode unitary nonlinear coupling gate l in layer d is defined as,

$$V_{l,d} = e^{-i\Delta t_d H^{(2)}(J_{l,d}, U)}, \quad (5)$$

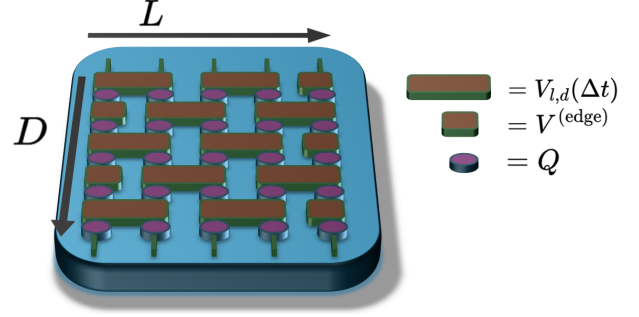


Figure 2: The qPIC setup. The circuit contains L waveguides with unitary coupling gates $V_{l,d}(\Delta t)$ 5, stacked in a bricked pattern of layer depth D , with unitary edge gates $V^{(\text{edge})}$ (brown rectangles). Each layer of unitary gates, is followed by non-unitary stochastic sampling gates Q (Eq. (13)) for the losses (purple dots).

with $H^{(2)}(J, U)$ defined in Eq. (2), $J_{l,d}$ the gate coupling rate and U the gate nonlinearity, constant across the circuit. The gate time is given as $\Delta t_d = \Delta z_d / v_g$, with v_g the polariton group velocity and Δz_d the spatial length of layer d .

At the edges of the circuit, where no two-mode gate is overlapping with the edge waveguide, a single-mode unitary gate $V_d^{(\text{edge})} = e^{-i\Delta t_d H^{(\text{edge})}}$ is applied, with $H^{(\text{edge})} = (U/2)a^\dagger a^2$, thus ensuring a constant intra-waveguide nonlinearity across the circuit.

Unless mentioned otherwise, each waveguide l in the circuit receives as input uncoupled coherent laser light, defined by the complex parameter α_l , which exhibits Poissonian photon number statistics, uncorrelated between different modes l ,

$$|\psi\rangle_{\text{in}} = \bigotimes_{l=0}^N |\alpha_l\rangle, \quad (6)$$

with,

$$|\alpha\rangle = e^{\alpha a^\dagger - \alpha^* a} |0\rangle = e^{-\frac{|\alpha|^2}{2}} \sum_i \frac{\alpha^n}{\sqrt{n!}} |n\rangle. \quad (7)$$

Whenever $U > 0$, the nonlinearity in the qPIC disrupts the Poissonian photon statistics, giving rise to nonclassical features in the photon number statistics of the output signal.

For bosonic states, a truncation \mathcal{N}_{max} in Fock number space is needed to represent the photon field in one single mode; this is the physical tensor dimension. The full Hilbert space required for simulating L photonic modes is then $\mathcal{D} = \mathcal{N}_{\text{max}}^L$, which, as expected, grows exponentially in the number of modes and quickly surpasses computational limits. Another approach is provided by

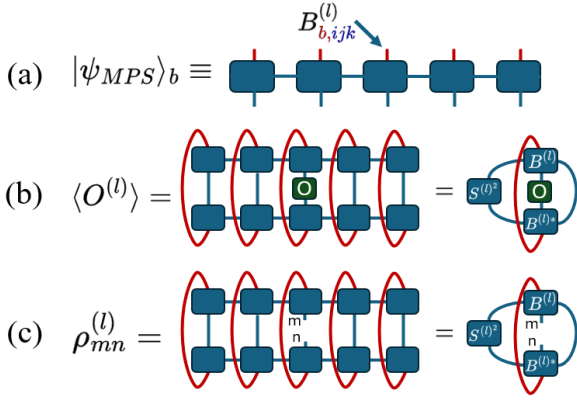


Figure 3: The MPS representation of the MC ensemble of quantum states. (a) Each site tensor is augmented with a fourth index b (red), which labels the batch in the Monte Carlo trajectory ensemble. (b) The tensor contraction for evaluating a local expectation value of a Hermitian operator O in mode (waveguide) l ; the MPS is contracted with its conjugate, with the O sandwiched in between in mode l . (c) The contraction for obtaining the reduced density matrix of mode l , $\rho^{(l)}$. (b)-(c) Thanks to the MPS being in right-canonical form, the circuit contraction is local, using the singular values stored in $S^{(l)}$.

1D tensor networks (tensor trains); the matrix product state (MPS) representation [39],

$$|\psi_{\text{MPS}}\rangle = \sum_{\{n\}} \text{Tr}[B_{n_1}^{(1)} B_{n_2}^{(2)} \dots B_{n_L}^{(L)}] |n_1 n_2 \dots n_L\rangle, \quad (8)$$

with $|n_1, n_2, \dots, n_L\rangle$ a multimode photon number Fock state. To avoid the cumbersome procedure of writing out all tensor indices, this is often represented as a tensor diagram, as illustrated in Fig. 3(a).

The quantum state in MPS form (8) is represented by a train of rank-3 tensors $B_{i,j,k}^{(l)}$. Here, the indices i and k the *bond* indices whose dimensions are limited by a chosen cutoff parameter χ_{max} , while j labels the truncated Fock space of dimension \mathcal{N}_{max} used to represent the photonic mode. The bond indices i, k encode the Hilbert-Schmidt decomposition across a bipartite cut in the tensor chain, and their dimensions, constrained by χ_{max} , determine the amount of entanglement that can be faithfully captured within the MPS representation [23]. For convenience, the MPS is kept in *right-canonical* form, which means that, when indices (j, k) are grouped together, the reshaped matrices $B_{i,(jk)}^{(l)}$ are right-unitary.

In Fig. 4, the differentiable method for contracting a circuit gate $V_{l,d}$ with on a photonic MPS state is shown. Contracting a two-mode nonlinear circuit gate $V^{(l,d)}$, represented as a rank-4 tensor, with waveguides $B^{(l)}$ and $B^{(l+1)}$, results in a rank-4 tensor $\Theta^{(l,l+1)}$. Using singular-value decomposition (SVD), the $\Theta^{(l,l+1)}$ tensor is decomposed into two rank-3 tensors, of which the latter is right-unitary. An ordered set of left-singular values $s_i^{(l)}$, representing the Schmidt coefficients of a bipartite decomposition across mode l , are stored in memory for later use. Iterating from right to left through the chain, contracting the unitary gates $V^{(l,d)}$, results in an updated right-canonical MPS $|\psi_d\rangle$ after application of circuit layer d . See Ref. [23], in which the circuit contraction method was presented, or Refs. [40, 39] for a full review. The open-source code provided by TeNPy [41] served as a reference for implementing the two-mode gate contraction efficiently in PyTorch.

An important note: Although the SVD steps in the circuit contraction are fully differentiable, implementing their gradients for complex-valued matrices (especially when they are close to degeneracy) can be prone to instabilities during the process of gradient backtracking. For the purposes of qPIC optimization, the PyTorch SVD module was overwritten, using the analysis from Ref. [42], with the necessary amendment of (i) adding explicit SV truncation in the gradient tracking and (ii) regularizing nearly degenerate SVs (the Hilbert-Schmidt coefficients of a bipartite decomposition) – see source files in [32].

3.2 Circuit dissipative losses using Monte Carlo trajectory sampling

The dominant component of circuit dissipation are photonic and excitonic losses, which are caused by material defects and nonradiative exciton recombination [43]. We rely on the Monte Carlo quantum trajectory method for stochastically sampling the impact of bosonic loss events on the photonic quantum state. The method was originally presented, independently, in Refs. [24, 25, 26] – see Ref. [27] for a comprehensive review, which also addresses the implementation using MPS.

In short, dissipative noisy quantum dynamics is generally described by the Lindblad master equation, which acts on the level of a quantum

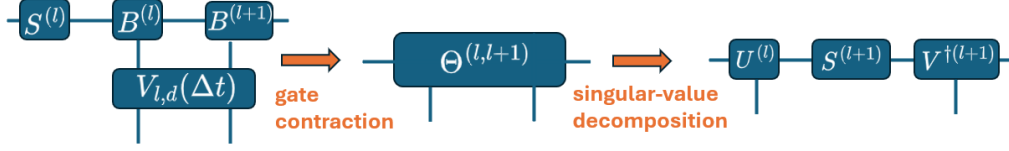


Figure 4: Applying a two-mode unitary gate in layer d , $V_{l,d}$, to the MPS state $|\psi_{d-1}\rangle$, exiting layer $d-1$, on mode l . First, the unitary gate tensor is contracted with the MPS tensors at site l and $l+1$. Next, the resulting rank-4 tensor $\theta^{(l,l+1)}$ is decomposed into two new rank-3 tensors using SVD. Both the tensor contraction and the SVD decomposition are differentiable tensor operations, of which the gradients can be tracked for evaluating gradients toward circuit parameters after full circuit contraction.

density matrix ρ [22],

$$\partial_t \rho = \frac{i}{\hbar} [\rho, H(t)] + \sum_i c_i \rho c_i^\dagger - \frac{1}{2} (c_i^\dagger c_i \rho + \rho c_i^\dagger c_i). \quad (9)$$

The first term on the r.h.s. contains the unitary evolution under the time-dependent Hamiltonian $H(t)$ of the statistical ensemble of quantum states, as represented by the density matrix ρ . The second term describes the Markovian dissipation generated by the dissipators c_i . For photonic losses, these are represented as $c_l \equiv \sqrt{\gamma} a_l$, that is, uncorrelated bosonic loss (annihilation) events in waveguide l , at a uniform rate γ . The dissipative part of Eq. 9 consists of two terms; $\frac{1}{2} \sum_l (c_l^\dagger c_l \rho + \rho c_l^\dagger c_l) = \frac{1}{2} \sum_l \{c_l^\dagger c_l, \rho\}$, with $\{\cdot\}$ being the anticommutator, can, equivalently, be absorbed in the first term by defining a non-Hermitian Hamiltonian $\tilde{H} = H - \frac{i}{2} \sum_i c_i^\dagger c_i$. The quantum noise is described by the dissipative *jump* term $\sum_i c_i \rho c_i^\dagger$, which can be, either, integrated deterministically in the master equation (9), or, alternatively, be sampled stochastically using an ensemble of pure-state Monte Carlo trajectories $|\psi^{(b)}(t)\rangle$. The latter option is the method we use in this work.

The Monte Carlo procedure is as follows; N_s trajectory states $|\psi^{(b)}(t=0)\rangle$, labeled with batch index b , are initiated – each initial batch state is identical if the system starts from a pure state, as holds for uncoupled coherent laser light described in Eq. (6). Next, each differential time step Δt , (i) the state $|\psi^{(b)}\rangle$ is unitarily evolved with $H(t)$ and (ii) the probability of a dissipative “click” is evaluated for a photon loss event in waveguide l ,

$$\Delta p_l^{(b)}(t) = \gamma \Delta t n_l^{(b)}(t), \quad (10)$$

with $n_l^{(b)}(t) = \langle \psi^{(b)} | a_l^\dagger a_l | \psi^{(b)} \rangle$. The probability $\Delta p_l^{(b)}(t)$ is, as is expected for Poissonian loss statistics, to first order proportional to (i) the

rate and time step, $\gamma \Delta t$, and (ii) the photonic occupation at time t of ensemble batch state b in waveguide l , $n_l^{(b)}(t)$.

After drawing a uniform random number $0 \leq r_l^{(b)} \leq 1$, there are two possible outcomes,

- $r^{(b)} \leq \Delta p_l^{(b)}(t)$: Apply the jump, $|\psi^{(b)}(t)\rangle \leftarrow a_l |\psi^{(b)}(t)\rangle$. Physically, this represents the detection of an emitted photon by an observer in time interval $[t, t + \Delta t]$ and, henceforth, a corresponding photon subtraction inside the waveguide l .
- $r^{(b)} > \Delta p_l^{(b)}(t)$: Perform a non-unitary time step, $|\psi^{(b)}(t)\rangle \leftarrow e^{-\frac{\gamma \Delta t}{2} a_l^\dagger a_l} |\psi^{(b)}(t)\rangle$. Physically, this step encodes the information gathered by an external observer by *not* detecting an emitted photon in time interval $[t, t + \Delta t]$. This makes the observer assume that $|\psi^{(b)}\rangle$ is in a state of lower photon occupation in waveguide l , as represented by the exponential suppression of higher photon amplitudes.

Both outcomes are, in general, non-unitary, implying that the state $|\psi^{(b)}\rangle$ must be renormalized after application, before the next time step can be evaluated.

From the ensemble of trajectory states, the generally non-pure density matrix of the system is reconstructed at each time as,

$$\rho(t) \approx \frac{1}{N_s} \sum_{b=1}^{N_s} |\psi^{(b)}(t)\rangle \langle \psi^{(b)}(t)| \quad (11)$$

While the full density matrix is rarely explicitly evaluated, it is important that operator expectation values are, likewise, evaluated from the trajectory ensemble as,

$$\langle O(t) \rangle \approx \frac{1}{N_s} \sum_{b=1}^{N_s} \langle \psi_b(t) | O | \psi_b(t) \rangle. \quad (12)$$

For local few-body observables, the convergence is generally much faster than the full density matrix [27].

Within the MPS representation of the quantum state (8), the default rank-3 tensors, are expanded by adding the ensemble batch index b for representing the ensemble of Monte Carlo trajectory states – see Fig. 3(a). A local operator expectation value in waveguide l is evaluated by the contraction of the MPS state with its conjugate, with the local operator O contracted in between, as shown in Fig. 3(b). The single-mode reduced density matrix of mode l can be obtained in the same way, but now the physical indices of mode l are left open, as shown in 3(c). In all panels, the red indices are the added batch indices of the stochastic ensemble. Contracting the batch indices of a state with the batch indices of its conjugate, provides the ensemble average in the Monte-Carlo trajectory quantum simulation of dissipative dynamics from Eqs. (11)-(12) upon normalization. On the right side of 3(b)-(c), we illustrate that, since the MPS is kept in right-canonical form, contracting sites right from mode l results in the identity matrix, while left from l requires the contraction of the singular values, which are stored in memory after the two-mode gate contractions. Hence, only a local contraction must be performed to obtain local quantities $\langle O^{(l)} \rangle$ or reduced density matrices $\rho^{(l)}$.

For simulating the stochastic sampling of the Monte-Carlo trajectories using the tensor network representation of the qPIC, a single-mode non-unitary gate is introduced,

$$B_{l,km}^{(b)} \leftarrow \sum_j Q_{l,ij}^{(b)} B_{l,kjm}^{(b)}, \quad (13)$$

with,

$$Q_l^{(b)} = a \text{ if } r_l^{(b)} \leq \gamma \Delta t n_l^{(b)} \text{ else } e^{-\frac{\gamma \Delta t}{2} a^\dagger a}, \quad (14)$$

with a (a^\dagger) the bosonic annihilation (creation) operator and r_b an array of uniformly distributed random number between 0 and 1, sampled independently for any trajectory state b , conform the method presented in Ref. [25]. Since the stochastic gate $Q_{l,ij}^{(b)}$ is non-unitary, it breaks the right-canonical MPS form, which must be restored after the contraction of Eq. (13).

When including the dissipation process $Q_l^{(b)}$ in Eq. (13), the computational workload significantly increases because of two reasons,

1. A Monte Carlo ensemble needs to be evaluated and sampled, which causes a linear increase in the workload. This can be sampled *embarrassingly parallel* on separate cores, as was previously illustrated in, e.g., Refs. [44, 28]. For this work, however, we prioritize maintaining the tensor structure for efficient gradient tracking. We do this by expanding the default MPS representation with a batch index, as illustrated in Fig. 3, and use GPU tensor processing provided by the Python library PyTorch [45].
2. The non-unitary gates $Q_l^{(b)}$ require the reformatting of the MPS in right-canonical form after application. This involves a sequence of QR and SVD decompositions (see procedure in Ref. [23] or the source code from Ref. [41]), which, not surprisingly, significantly increases the workload for (i) the circuit evaluation and (ii) the computational steps needed for backtracking the gradients towards the qPIC variables $J_{l,d}$.

3.3 Gradient-based optimization scheme for qPICs

For the optimization, a real-valued differentiable figure of merit (FOM) is defined on the circuit output quantum state $|\psi_{\text{out}}\rangle$,

$$\mathcal{L}(\{J_{l,d}\}) := \mathcal{L}[|\psi_{\text{out}}(\{J_{l,d}\})\rangle]. \quad (15)$$

The FOM depends on the set of gate coupling variables $\{J_{l,d}\}$, of which the gradients towards each coupling parameter $\partial \mathcal{L} / \partial J_{l,d}$ are tracked using the autograd provided by PyTorch. More specifically, we use the Adam optimizer [46] to make gradient-based updates of the variables $J_{l,d}^{(i)}$, with i the index of the iteration, starting from some initial condition $J_{l,d}^{(\text{init})} := J_{l,d}^{(i=0)}$. After iterative circuit contraction and FOM evaluation, $\mathcal{L}^{(i)}$ converges and optimal coupling rates are found; $\{J_{l,d}^{(\text{opt})}\} := \text{argmin}_{\{J_{l,d}\}} [\mathcal{L}(\{J_{l,d}\})]$. A maximal number of iterations $\mathcal{N}_{\text{iter}}$ can be set to control the total runtime.

We note that the Markovian Monte-Carlo trajectory click probabilities $\Delta p_l^{(b)}(t)$ themselves (Eq. (10)) are not explicitly included in the gradient backtracking algorithm, only the outcomes in terms of the gate tensor contractions $Q_{b,ij}$ of the different batch states (see Eq. (13)). In that

regard, we consider variations of $\Delta p_l^{(b)}(t)$ induced by updates of the gate couplings $J_{l,d}^{(i)}$ across subsequent iterations i negligible for the backtracking.

In what follows, we formulate the FOMs \mathcal{L} for two use-cases that have a direct relevance for practical implementation with integrated photonics for near-term quantum processing, quantum state generation (Sec. 4) and optimal readout of quantum phase sensing (Sec. 5). In the first case, the goal is to approach a target single-mode quantum state as close as possible in the circuit output mode. In the second, we maximize the qPIC sensitivity towards a small phase shift in one of the incoming coherent light sources.

4 Quantum state generation

Exciton-polaritons in GaAs structures have emerged as a versatile platform for exploring quantum state generation and manipulation. Their unique light-matter duality enables coherent control and nonlinear interactions, which are crucial for developing quantum technologies. Recent works have demonstrated the potential of exciton-polariton systems in implementing quantum neuromorphic platforms that exploit reservoir computing principles for efficient quantum state preparation, reconstruction, and processing [47, 48, 49].

The objective for the task of quantum optical state preparation is optimizing the circuit gate architecture for generating a target outcome state, $\rho^{(\text{tar})}$, in one circuit mode l (single-mode case) or, more generally, a set of output modes $l_0 \dots l_k$ (multi-mode case). Here, we concentrate on the single-mode case, but generalizing the procedure to multi-mode state generation is straightforward.

The starting point for the circuit optimization is the photonic input of uncoupled coherent laser light, as defined in Eq. (6). We set the amplitude uniform across all waveguides, i.e., $\forall l : \alpha_l \equiv \alpha$.

4.1 The figure of merit for state preparation

After contracting the circuit tensor gates, the output MPS is obtained. For the single-mode case, simple contraction of the right canonical MPS gives the single-mode density matrix $\rho_{mn}^{(l)}$ of output mode l – see Fig. 3(c). We define the FOM as the weighted trace distance between $\rho^{(l)}$ and

the target state $\rho^{(\text{tar})}$, defined as follows,

$$\begin{aligned} \mathcal{L}_\rho &= T_{\mathcal{M}}[\rho^{(l)}, \rho^{(\text{tar})}] \\ &= \frac{1}{2} \text{tr} \left[\sqrt{\delta \rho_{\mathcal{M}}^{(l)\dagger} \delta \rho_{\mathcal{M}}^{(l)}} \right] \\ &= \frac{1}{2} \sum_{r=1}^{\mathcal{N}_{\max}} |\lambda_r|, \end{aligned} \quad (16)$$

with $\delta \rho_{\mathcal{M}}^{(l)} = \mathcal{M} \odot (\rho^{(l)} - \rho^{(\text{tar})})$ and λ_r its eigenvalues. \mathcal{M} is a normalized “mask”, of which the Hadamard (dot) product gives weights to individual matrix elements of $\rho^{(l)}$ for the optimization scheme. For example, diagonal elements, representing classical probabilities, could be given higher relative weight, or lower weight can be assigned to the vacuum $\rho_{00}^{(l)}$; exceedingly occupying the vacuum can be tolerated, as this limits the generation of spurious nonzero signals when no direct match is possible. Indeed, with conditional sampling (only nonzero signals are counted) the vacuum mode is easily filtered out in experimental sampling runs.

As initial condition, the optimization starts from nearly uncoupled waveguides, set as $J_{l,d}^{(\text{init})} = 0.01$, so that the coherent uncoupled input state (Eq. (6)) is contracted to a (near) zero-entanglement, separable circuit output state, well contained in the variational manifold set by the control parameter $\chi_{\max} = 500$. During the optimization, the gate couplings are constrained to be positive, with at most a full rotation from one waveguide to the other and back; $0 \leq J_{l,d} \Delta t \leq \pi$. The couplings $J_{l,d}$ will gradually increase or damp out to zero across subsequent iterations of optimization. As additional constraint, we impose a regularization to avoid an unconstrained growth of the couplers between different iterations of optimization. Physically, this is justified by considerations related to chip fabrication; limiting the amount of nonzero couplers is beneficial. Indeed, couplers are sensitive to fabrication errors when two neighboring waveguides must approach each other at the correct separation (see simulation in Appendix A). On the other hand, this ensures numerically that the initial state remains well within the limits posed by the maximal MPS bond dimension, χ_{\max} .

The Von Neumann entropy entanglement of bipartite chain divisions is directly accessible, thanks to the MPS being in right-canonical form, from the singular values stored in memory after

two-mode gate contraction. This provides an adequate measure for regularizing $J_{l,d}$ in order to prevent unconstrained growth of the tensor bond dimensions χ_l . To this end, we include in the FOM a measure for reducing Von Neumann entropy,

$$\mathcal{L}_S = \sqrt{\sum_{K=1}^L (S_{VN}^{(K)})^2}, \quad (17)$$

with,

$$\begin{aligned} S_{VN}^{(K)} &= -\text{tr}[\rho^{(l \leq K)} \ln \rho^{(l \leq K)}] \\ &= -\sum_{k=0}^{\chi_K} (s_k^{(K)})^2 \ln (s_k^{(K)})^2, \end{aligned} \quad (18)$$

with L the number of waveguides (modes) and $\rho^{(l \leq K)}$ the reduced density matrix of modes left from waveguide K ($l \leq K \leq L$). $S_{VN}^{(l)}$ is the bipartite entanglement entropy and χ_K the bond dimension (number of singular values), with $s_k^{(K)}$ the k -th left singular value of mode $K+1$. An extra (trivial) averaging over entanglement profiles must be done for the set of batch ensemble states in the Monte Carlo trajectory description.

Finally, the full FOM for optimizing state preparation is given as,

$$\mathcal{L}_{\text{tot}} = \lambda_\rho \mathcal{L}_\rho + \lambda_S \mathcal{L}_S, \quad (19)$$

with λ_ρ the weight for the density matrix matching and λ_S the weight for regularizing the state bipartite entanglement. We set $\lambda_\rho = 1 - \lambda_S$, as only the relative weight matters. For this use-case, the weights were picked empirically by hand, based on the system size L and circuit depth D . As a control mechanism, the maximal bond dimension reached in the MPS was monitored, for a singular-value cutoff of $s_{\min} = 10^{-6}$, to ensure that it remains well below $\chi_{\max} = 500$ – the maximal value encountered was $\chi_l = 325$.

4.2 Case 1: Deep-circuit unitary cat-state generation

We propose optimized qPICs to generate Schrödinger cat states, defined as,

$$|\text{cat}_\pm\rangle = N(|\beta\rangle \pm |-\beta\rangle), \quad N = \frac{1}{\sqrt{2(1 \mp e^{-2|\beta|^2})}}, \quad (20)$$

in the near-infrared regime, typical for excitons in GaAs samples, useful for fiber-based quantum networks. The even state $|\text{cat}_+\rangle$ only has

even photon number occupation, while the odd state $|\text{cat}_-\rangle$ only has odd occupation. Cat states are crucial quantum resources in photonics due to their nonclassical superposition, which enhances quantum sensing, metrology, and information processing [50], while showing robustness to phase noise [51]. The experimental preparation in optics is traditionally via photon number states and homodyne detection [52].

In this use-case, we demonstrate the optimization of odd cat-state preparation with $\beta = 1$ (Eq. (20)) in the middle output of the circuit – waveguide index $l = (L-1)/2$ for odd number of waveguides, or $l = L/2$ if even. For the optimization, the FOM from Eq. (19) is used, with $\lambda_S = 5 \cdot 10^{-3}$. In the weighted trace distance from Eq. (16), a low weight is given to the vacuum mode $\rho_{00}^{(l)}$, by setting \mathcal{M}_{00} a factor 9 lower than other weights $\mathcal{M}_{(ij) \neq (00)}$. The maximal photon occupation is $N_{\max} = 5$, giving a physical dimension of $d = 6$, and a learning rate of 0.1 was used for the Adam optimizer. Coherent states of amplitude $\alpha = 1$ are injected, so on average one photon per waveguide.

In Fig. 5 the results are shown for cat-state generation as a function of (i) number of circuit waveguides, (ii) circuit depth and (iii) circuit accumulated nonlinearity $U \cdot T_{\text{circ}}$, with T_{circ} the total time photons need to pass through the circuit. Points with the same $U \cdot T_{\text{circ}}$ (lying above each other) have the same circuit spatial extent, but that length is subdivided in a different number of layers D , thereby reducing the gate times Δt proportionally. Therefore, higher D offers more optimization “flexibility” for the couplers $J_{l,d}$ while preserving the circuit nonlinearity $U \cdot T_{\text{circ}}$. For example, using a realistic baseline for the parameters, if the full circuit has $T_{\text{circ}} = 2.5 \text{ mm} \cdot v_g^{-1}$, with v_g the polaritonic group velocity, that means that for depth $D = 25$ this would be a stack of layers of $100 \mu\text{m}$ each, while $D = 5$ would give $500 \mu\text{m}$. To convert length scales to time units, we set v_g a factor 2 lower than the speed of light in GaAs, $0.5c/n_{\text{GaAs}} \approx 0.5 \mu\text{m} \cdot \text{ps}^{-1}$, equivalent to 0.5 exciton fraction – see Sec. 2. This allows us to obtain dimensionful units for the photonic nonlinearity; e.g., $U \cdot T_{\text{circ}} = 0.1$, leads to $U = 5 \cdot 10^{-4} \text{ ps}^{-1} = 0.34 \mu\text{eV}/\hbar$, in turn corresponding to a 2D material nonlinearity $g = U \cdot S_{\text{pulse}} = 48 \mu\text{eV} \cdot \mu\text{m}^2$, if the pulse associated surface is $141 \mu\text{m}^2$ – see estimate in

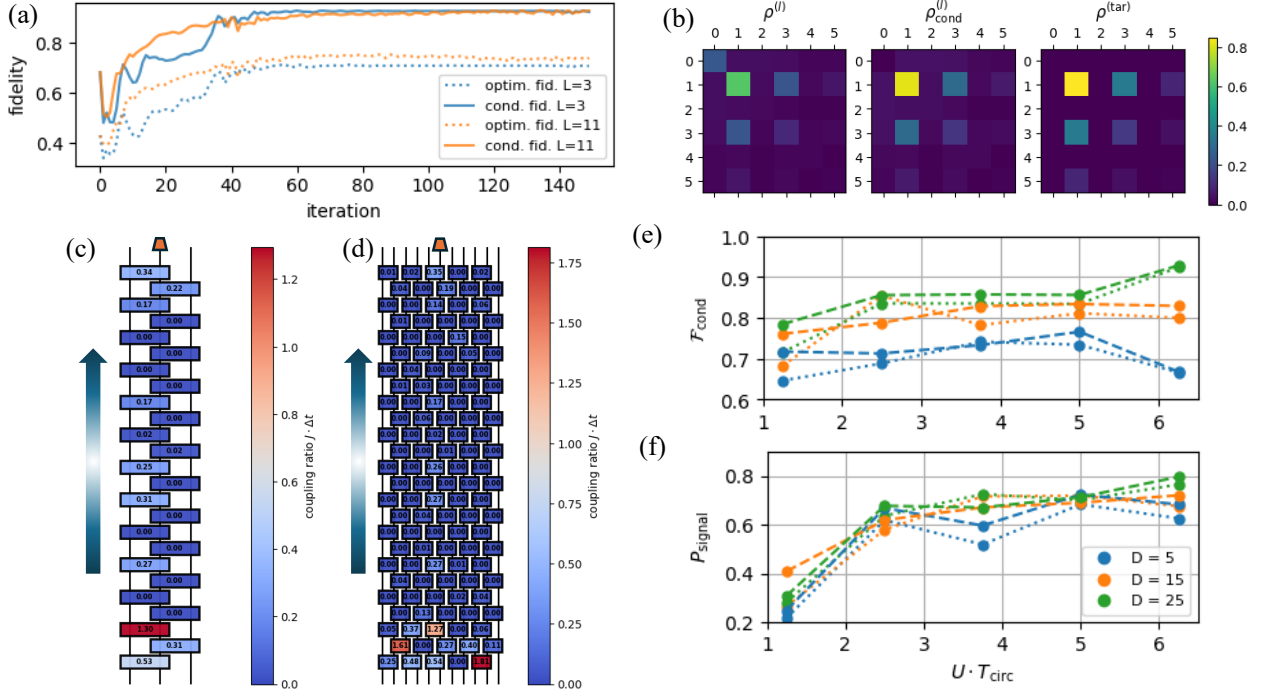


Figure 5: The results for cat state preparation. (a) The fidelity converges for $L = 3$ (blue) and $L = 11$ (orange), for both the optimization fidelity (dotted) and conditioned fidelity (full). (b) The density matrix obtained and compared with $\rho^{(\text{tar})}$ for $L = 3$, both the unconditioned and conditioned. (c)-(d) The optimized circuits obtained, for $L = 3$ and $L = 11$, respectively, with circuit nonlinearity $U \cdot T_{\text{circ}} = 6.25$. (e)-(f) The conditioned fidelity (e) and generation probability (f) as function of circuit accumulated nonlinearity, for $L = 3$ (dotted) and $L = 11$ (dashed lines), for different circuit depths D .

Appendix A, below Eq. (39).

In Fig. 5(a) the achieved state fidelity,

$$\mathcal{F}(\rho) = \left(\text{tr} \sqrt{\sqrt{\rho}(\rho^{(\text{tar})})\sqrt{\rho}} \right)^2, \quad (21)$$

is shown after i iterations, for a narrow circuit of $L = 3$ and a wide circuit with $L = 11$ waveguides. We show $\rho^{(i)}$, having nonzero occupation of the vacuum mode due to the lower weight given in \mathcal{M}_{00} (dotted lines), and the corresponding conditioned fidelity $\mathcal{F}_{\text{cond}}$, obtained after filtering out the vacuum occurrences (i.e., setting $\rho_{0i}^{(i)} = \rho_{i0}^{(i)} = 0$) and renormalization (full lines). As expected, the conditioned fidelity is significantly higher. In Fig. 5(b) the obtained density matrix for $L = 3$ is illustrated and compared with the target $\rho^{(\text{tar})} = \rho_{\text{cat-}} = |\text{cat-}\rangle\langle\text{cat-}|$, for which a conditioned fidelity of $> 90\%$ is obtained for deep circuits of $D = 25$. In Fig. 5(c)-(d), the optimized circuits are displayed, with the color codes representing the coupling strength of the gates. It is clear that, for the case $L = 11$ (Fig. 5(d)), a large part of the gates converge to (near-) zero coupling (dark blue gate components), therefore

only accumulating intra-waveguide nonlinearity. Indeed, the fidelity obtained for $L = 3$ (Fig. 5(c)) is nearly identical, and we see that the gates on the right side in the middle, which couple the second and third waveguide, converge to zero coupling $J\Delta t = 0$, while the left ones generate the optimal two-mode interferences. In conclusion, we observe that for single-mode odd cat state generation, fine-tuned interferences and accumulated Kerr-nonlinearity using three waveguides suffices to stabilize accurate odd cat-state photon statistics. In Fig. 5(e)-(f), the conditioned fidelity (Fig. 5(e)) and obtained probability P_{signal} for cat-state generation (Fig. 5(f)) is shown as a function of accumulated circuit nonlinearity $U \cdot T_{\text{circ}}$, for different circuit depth (number of layers, color codes) and number of waveguides, $L = 3$ (dotted) and $L = 11$ (dashed).

Generally, the flexibility offered by circuits subdivided in larger number of layers D leads to higher fidelities and probability of generation. In Fig. 5(f), we observe that, while the conditioned fidelity for $L = 3$ and $L = 11$ is similar, the probability of odd cat-state signal, $P_{\text{signal}} = 1 - \rho_{00}$,

is about 3% higher for $L = 11$ ($P_{\text{signal}} = 0.797$) than for $L = 3$ ($P_{\text{signal}} = 0.765$) for the case of high nonlinearity, $U \cdot T_{\text{circ}} = 6.25$. However, the statistical significance of this finding is, arguably, rather limited.

In Appendix D, we analyze in detail the circuit robustness towards small fabrication errors in the couplings $J_{l,d}$. As a result, there is no discernible benefit found for robustness of $L = 11$ circuits w.r.t. $L = 3$. This brings us to the conclusion that the accumulated nonlinearity is of primary importance for odd cat-state generation. Next to that, larger layer division D helps to approach better optimal sequences of interferences between linear inter-waveguide couplings and intra-waveguide nonlinear phase shifts. No immediate benefit is found for scaling up to qPICs beyond $L = 3$ waveguides. Perhaps this changes if circuit robustness is incorporated as an explicit requirement in the FOM for state optimization (19), as was studied, e.g., in Ref. [53] for neuromorphic optical computing.

4.3 Case 2: Noisy maximization of antibunched statistics and single-photon efficiency

Single-photon generation in the near-infrared regime is a key quantum resource for photonic quantum technologies and fiber-based communication. Such sources are generally realized via solid-state quantum emitters, defects in crystals, or nonlinear optical processes, enabling on-demand generation of pure single photons with high indistinguishability and brightness – see Ref. [54] for an overview. In this realm, strong antibunched photon statistics, characterized by the second-order correlation function $g^{(2)}(0) := \langle :n^2: \rangle / \langle n \rangle^2 < 1$, is a landmark for identifying nonclassical sources of light, ensuring the suppression of multi-photon events and high quantum fidelity. Generally, any measured value of $g^{(2)}(0) < 1$, detectable within error bars, is considered a valid signature of “nonclassicality” of the photon statistics and a path towards photon blockade [13].

For the use-case of single photon generation in a noisy environment, we demonstrate the optimization scheme with the explicit inclusion of the stochastic Markovian loss processes. As previously outlined in Sec. 3.2 (see Fig. 3), the MPS tensors $B_{l,ijk}$, with l the waveguide mode index, are expanded in rank from 3 to 4, with

an additional batch index b ; $B_{l,ijk}^{(b)}$. This index serves for sampling the outcomes of the non-unitary stochastic gates $Q_l^{(b)}$ (Eq. (13)). The computational complexity increases for two reasons; (i) the added batch dimension and (ii) the contraction of non-unitarity single-mode gates $Q_{b,ij}$, which disrupts the canonical MPS form (Eq. (13)).

Our objective is to optimize the qPIC design under the practical constraints of fabrication techniques that are currently accessible, with the near-term goal of experimentally observing nonclassical photon statistics in waveguide-integrated polariton systems. To this end, we include as FOM the minimization of the second-order correlation function $g^{(2)}(0)$ for a chosen circuit output l :

$$\mathcal{L}_g := g_{ll}^{(2)}(0) = \frac{\langle a_l^\dagger a_l^\dagger a_l a_l \rangle_{\text{out}}}{\langle a_l^\dagger a_l \rangle_{\text{out}}^2}, \quad (22)$$

where $\langle O \rangle_{\text{out}} := \langle \psi_{\text{out}} | O | \psi_{\text{out}} \rangle$. In addition to this, we include the minimization of the single-photon density-matrix trace distance, as defined in Eq. (16), with $\rho_{11}^{(\text{tar})} = 1$, $\rho_{(ij) \neq (11)}^{(\text{tar})} = 0$, leading to the FOM,

$$\mathcal{L}_{\text{tot}} = \lambda_\rho \mathcal{L}_\rho + \lambda_g \mathcal{L}_g \quad (23)$$

A larger weight was given to minimizing density-density correlations, $\lambda_g = 0.9$ in comparison with the trace-norm single-photon matching, $\lambda_\rho = 0.1$. Assuring $\lambda_\rho \neq 0$ secures that the mode l does not converge to a value arbitrarily close to vacuum output for low nonlinearity U , as is generally seen in works on the *unconventional photon blockade* – see, e.g., Refs. [55, 56].

Similar as for cat state generation (Sec. 4.1), we consider a circuit architecture, now consisting of $L = 5$ waveguides, subdivided in D layers, with a circuit accumulated non-linearity $U \cdot T_{\text{circ}}$ and T_{circ} the total circuit time, and the couplers are initially set to $J_{l,d}^{(\text{init})} = 0.01$. For this case, the entropy weight is largely irrelevant and set to zero. Indeed, a representation of the full Hilbert space of L bosonic modes with truncated Fock space \mathcal{N}_{max} and $L = 5$ modes requires a MPS tensor bond dimension in the middle of the chain of $\chi_{L/2} = d^2 = 36$, with $d = \mathcal{N}_{\text{max}} + 1 = 6$ the physical tensor dimension. Finally, similar as before, we set the weight for matching the vacuum mode, \mathcal{M}_{00} a factor 9 lower than other matrix elements in \mathcal{L}_ρ . Each optimization run was sampled

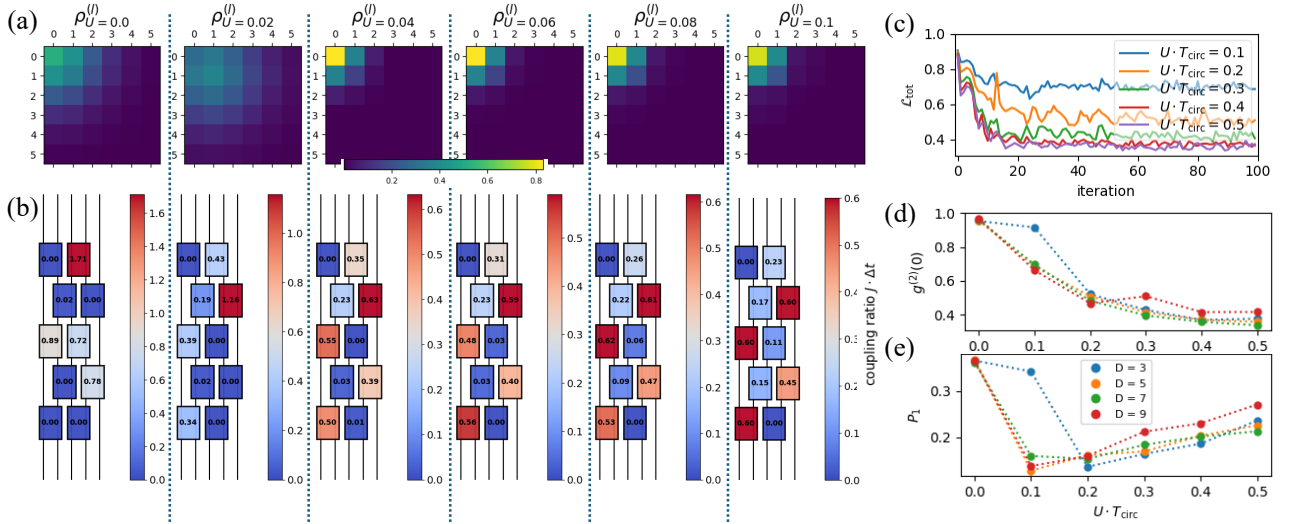


Figure 6: The results for noisy single-photon generation. (a)-(b) The obtained optimal density matrix (a) and corresponding optimal circuit (b), for different values of nonlinearity U . (c) The convergence of the FOM, for different values of U at $D = 5$. Due to the MC sampling ($N_s = 400$), some noise remains after convergence. (d) the optimal value for $g^{(2)}(0)$ and (e) the probability of single-photon generation, for different circuit divisions D (same color codes). Overall, higher $U \cdot T_{\text{circ}}$ leads to stronger antibunching and higher single-photon probability.

with $\mathcal{N}_s = 400$ stochastic sample states b , leading to a rank-4 MPS tensor representation with maximally $\mathcal{N}_s \cdot \chi_l^2 d \leq 400 \times 36 \times 6 \times 36 \approx 3 \cdot 10^6$ tensor elements.

In Fig. 6, the results for noisy qPIC optimization for single-photon generation are shown, scanning the circuit depth D and the accumulated nonlinearity $U \cdot T_{\text{circ}}$, with a constant loss rate of $\gamma \cdot T_{\text{circ}} = 0.5$ – that is, on average 60% of photons pass through circuit. To put it in numbers, if we set $T_{\text{circ}} = 500 \mu\text{m} \cdot v_g^{-1}$, we scan gate lengths from $166 \mu\text{m}$ ($D = 3$) to $56 \mu\text{m}$ ($D = 9$), with a decay time $\tau = 1/\gamma = 5 \text{ mm} \cdot v_g^{-1}$. If we set the circuit nonlinearity $U \cdot T_{\text{circ}} = 0.5$, the maximal value considered, the same values for circuit nonlinearity $\hbar U = 0.34 \mu\text{eV}$ and material 2D nonlinearity $g = 48 \mu\text{eV} \cdot \mu\text{m}^2$ are obtained as estimated in Sec. 4.1.

We present in Fig. 6 the obtained optimal density matrices (Fig. 6(a)) with the corresponding circuit configuration Fig. 6(b)), for increasing $U \cdot T_{\text{circ}}$, at $D = L = 5$. For higher $U \cdot T_{\text{circ}}$, the number distribution grows more concentrated around $n = 0$ and $n = 1$ photons, suppressing photon number states of $n \geq 2$, as expected for achieving low values of $g_u^{(2)}(0)$. Indeed, if exactly $\rho_{nn}^{(l)} = 0$ holds for all $n \geq 2$, we get perfect antibunched statistics, $g_u^{(2)}(0) = 0$ – see Eq. (22).

In Fig. 6(c), the curves of convergence of the FOM \mathcal{L}_{tot} from Eq. (19) are given for different

nonlinearities $U \cdot T_{\text{circ}}$ for circuit depth $D = 5$. After an initial stage of convergence (roughly the first 20 iterations), the optimal circuit shows statistical fluctuations in the semi-steady state it reaches in later iterations. Each iteration, a new batch of $\mathcal{N}_s = 400$ Monte Carlo states was sampled, independently of the previous batch. In Fig. 6(d)-(e), the mean second-order correlations $g^{(2)}(0)$ and single-photon probability $P_1 = \rho_{11}^{(l)}$ are shown, respectively, for increasing accumulated nonlinearity $U \cdot T_{\text{circ}}$ and varying circuit division D . The final 20 iteration were averaged out to obtain the data points. The second-order correlations $g^{(2)}(0)$ converges to similar values for the second-order correlation function at high nonlinearity, $g^{(2)}(0) \approx 0.4$, largely independent of circuit division depth D . From this we conclude that the circuit nonlinearity $U \cdot T_{\text{circ}}$ is the main factor for generating antibunched photon statistics and, to a much lesser extent, the flexibility offered by varying the couplers $J_{l,d}$, as quantified by the circuit depth D . When analyzing the single-photon output probability $P_1 = \rho_{11}$ (see Fig. 6(e)), the probability of single-photon generation increases roughly linearly with nonlinearity $U \cdot T_{\text{circ}}$. Furthermore, a small increase ($\sim 3\%$) is seen in the single-photon output probability for high-flexibility $D = 9$. Though, it should be noted that at $D = 9$ also $g^{(2)}(0)$ is slightly higher at higher nonlinearities $U \cdot T_{\text{circ}} \geq 0.5$. There-

fore, if given more flexibility, the FOM for single-photon generation, formulated in Eq. (26), gives preference to slightly higher probability of single-photon generation, at the cost of lower antibunching – for the initial condition J_{init} and weights λ_g and λ_p considered here.

In summary, qPICs with $L = 5$ waveguides were investigated for noisy single-photon generation using stochastic MC sampling methods. The focus was on a regime reachable with current experiments and fabrication methods – see, e.g. Ref. [2]. qPICs of total spatial extent $\sim 500 \mu\text{m}$ were considered as an experimental baseline and it was observed that the circuit accumulated non-linearity $U \cdot T_{\text{circ}}$ is of primary importance, much more than the flexibility in varying the gate couplings offered by an increased layer subdivision D . The observations were generated with $N_s = 400$ sample states to illustrate the effect of the noise in the statistical sampling. When N_s is increased further, the standard deviation reached after the initial convergence is expected to decrease as $1/\sqrt{N_s}$, as is the default for stochastic sampling [27].

5 Case: optimal readout for quantum Sensing

Quantum metrology and sensing [57, 58, 59, 60, 61] has numerous applications in a wide range of fields; among which, global positioning [62], gravitational-wave detection [63], biomedical applications [64] or chemical detection [65]. For quantum sensing, the purpose is to construct a quantum state, on which a small perturbation can be optimally detected with a positive operator-valued measure (POVM). Harnessing multipartite quantum statistics, bounds from classical detection statistics may be broken, thereby possibly reaching the Heisenberg quantum limit when an optimal measurement is performed on the quantum state. This is characterized by the classical vs. the quantum Cramer-Rao bound [66]. The high complexity of (i) state initialization, (ii) signal detection and (iii) measurement analysis for optimal quantum sensing has led to general optimization schemes [67], possibly including Bayesian optimization [68] or machine learning [69], also in optical setups [70, 71].

In this analysis, we focus on the task of signal detection, generated with an optimal qPIC

for the sensing of a small incoming phase perturbation in the regime of low-photon occupation, using the quantum statistics generated by a non-linear circuit gates coupling the integrated waveguides – see Fig. 7. Same as before, a set of uncoupled coherent in-phase signals (see Eq. (6)) enters the qPIC, but, for this case, one of the incoming signals is given a small phase shift to be sensed, possibly caused by a slight displacement of a reflective object (as illustrated in Fig. 7(a)), a perturbation in material refractive index, or a small variation in exciton Stark shift (see, e.g., Ref. [3]). The waveguides $1 \dots L - 1$ receive the same coherent in-phase laser input $|\alpha\rangle$, $\alpha_{l \geq 1} = 1$, while the first waveguide is slightly perturbed, with $\alpha_{l=0} = e^{i\theta}$ and θ infinitesimally small. We develop an optimization scheme for maximizing the sensitivity towards the phase θ of the first input mode $l = 0$ in the circuit output signal of the last output mode, $l = L - 1$. The regime of low-photon occupation is explicitly considered, with the injection of $|\alpha|^2 = 1$ photon on average per waveguide mode l . This is crucial in settings where high photon flux could damage sensitive samples, such as biological specimens, or where low-energy probes are needed to avoid perturbation.

5.1 The figure of merit for optimizing phase sensing

We consider maximizing the classical Fisher information (FI) of the photon number distribution of one single circuit output mode l ,

$$\text{FI}^{(l)}(\theta) \Big|_{\theta=0} = \sum_n P_n^{(l)}(0) \left(\partial_\theta \log P_n^{(l)}(\theta) \Big|_{\theta=0} \right)^2 \quad (24)$$

with $P_n^{(l)}(\theta) = \rho_{nn}^{(l)}(\theta)$, the photon number distribution of the final output $l \equiv L - 1$, conditioned on the input phase difference θ ($\theta = 0$ if unperturbed). The reduced density matrix of the waveguide mode, defined as $\rho^{(l)}(\{J_{l,d}\}) = \text{tr}_{l' \neq l} [\psi_{\text{out}}(\{J_{l,d}\})]$, is obtained from the tensor contraction of the qPIC output state – see Fig. 3(c).

The classical Fisher information provides an immediate bound on the variance for metrology of the variable θ from these measurement statistics [66],

$$(\Delta\theta)^2 \geq \frac{1}{m\text{FI}^{(l)}(\theta)} \geq \frac{1}{m\text{QFI}(\theta)}, \quad (25)$$

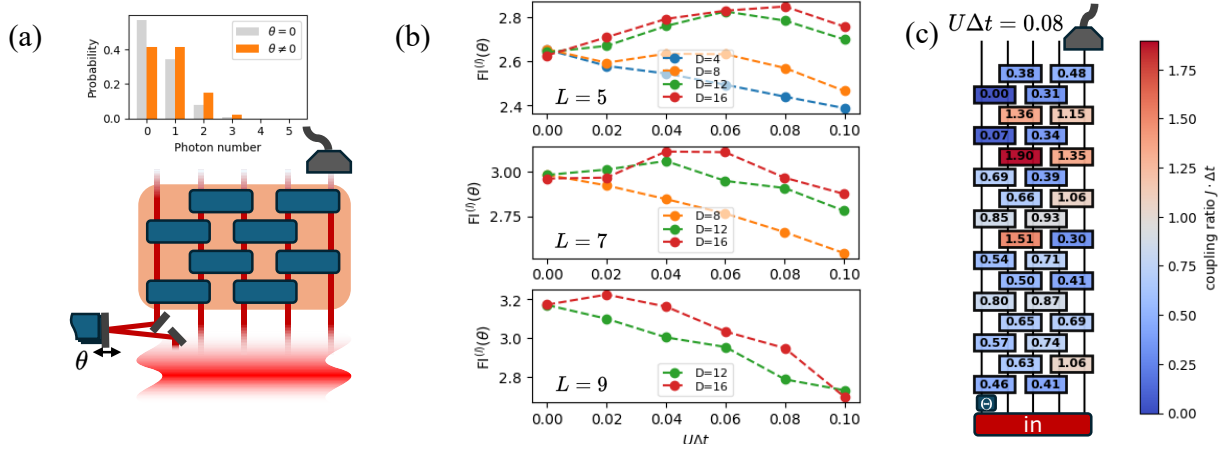


Figure 7: Circuit optimization applied to optimal readout for phase sensing. (a) an illustration of the setup, one input receives a phase shift from an object displacement, from one output the number distribution is used for detection. (b) the results for optimizing the measurement Fisher information for different waveguides, $L = 5$ (top), $L = 7$ (middle) and $L = 9$ (bottom) and different circuit depths (color codes). (c) a visualization of the optimal circuit obtained for $L = 5$ and $D = 16$, for $U\Delta t = 0.08$, a phase shift is given to the left input, while the readout is in the right output.

with the variance $\Delta\theta^2 = E[(\theta - \mu_\theta)^2]$ and m the number of independent statistical measurement samples – the number of pulses detected at the circuit output, in this case. $\text{QFI}(\theta)$ is the quantum Fisher information, which bounds the classical $\text{FI}(\theta)$ that can be extracted from a quantum state with a POVM. The Heisenberg limit for detection is saturated when the second bound in Eq. (25) is satisfied, i.e., $\text{FI}^{(l)}(\theta) \equiv \text{QFI}(\theta)$. For the case we are considering, $\text{QFI}(\theta)$ can be evaluated analytically from coherent state overlap and gives $\text{QFI}(\theta) = 4|\alpha|^2$ – see Appendix C.

Here, we want to maximize $\text{FI}^{(l)}(\theta)|_{\theta=0}$, for the purpose of minimizing the variance on detecting a small phase shift from $\theta = 0$, $(\Delta\theta)^2$, while approaching the Heisenberg limit as close as possible. In other words, the qPIC is optimized to emulate a Hermitian operator for measurement that maximizes the extraction of Fisher information $\text{FI}^{(l)}(\theta)$. For this, we formulate the FOM for optimizing phase-sensing qPIC readout as,

$$\mathcal{L} = \lambda_{\text{ps}}\mathcal{L}_{\text{ps}} + \lambda_S\mathcal{L}_S, \quad (26)$$

with $\mathcal{L}_{\text{ps}} = -\text{FI}^{(l)}$. Same as for state generation, the coupling rates $J_{l,d}$ are regularized by reducing the state bipartite entanglement, using the objective \mathcal{L}_S – see definition in Eq. (17).

5.2 Optimal readout for quantum phase sensing

In Fig. 7, we present the results obtained for optimizing the unitary qPIC for the task of quan-

tum phase sensing, without considering dissipation. In Fig. 7(a), the setup is illustrated, the left coherent input (index $l = 0$) is given a small phase shift and the qPIC and the distinguishability towards the number distribution of the last output (index $l = L - 1$) is maximized, using the FOM from Eq. (26). This way, the effect of multimode interferences is maximized as a starting condition, by the need for the signal to pass the circuit from left to right. The experimental signature for this is characterized by the classical Fisher information of one output's photon number distribution – see Eq. (24). The goal is to approach the quantum Heisenberg limit as close as possible, variationally within the qPIC architecture, as set by the quantum Fisher information (QFI). As derived in Appendix C, with $\alpha = 1$, this sets a bound of $\text{QFI} = 4$, so that $\mathcal{L}_{\text{ps}} \geq -4$. The results are shown in Fig. 7(b)-(c), for different circuit size $L \in \{5, 7, 9\}$ (up-down) and for different depth $D \in \{4, 8, 12, 16\}$, with $|\alpha| = 1$ across all inputs. Additionally, the initial condition for the couplers was set relatively high to start from large interferences, $J\Delta t = 0.3$ – remember, $J\Delta t = \frac{\pi}{4} \approx 0.78$ is a 50:50 coupler. Note that $D \geq L - 1$ must hold for the phase-shifted signal to be connected to the output measurement when trespassing the circuit.

We find that, for sufficiently deep circuits, the optimal Fisher information is obtained at nonzero nonlinearities, $U\Delta t > 0$. This is clearly

seen for $L = 5$ and $L = 7$, which have an optimum at depths $D = 12$ or $D = 16$ for higher, nonzero gate nonlinearities. Remarkably, this makes us conclude that, by gathering number outcome statistics in the low-photon occupation regime, it is not solely linear photonic interferences that realize maximal phase-shift sensitivity (as would be done, e.g., in standard homodyne detection schemes) but that higher circuit nonlinearity $U \cdot T_{\text{circ}} > 0$, with $T_{\text{circ}} = D\Delta t$, can surpass the classical limit of linear photonics at $U = 0$, where all circuit depths D coincide. When $U\Delta t$ becomes too high, effects of blockade, caused by the nonlinearity-induced blueshift, become dominant, as such reducing the qPIC phase sensitivity – see, e.g., the experimental results in [3].

In Appendix E, we explain in more detail that the optimal circuit sensitivity in the regime of low pulse photon occupancy can be understood, to a limited extent, from an analysis of Gaussian FI (see, e.g. Ref. [72]). It is shown that the Gaussian FI, given by $\frac{1}{\sigma^2}(\partial_\theta \mu)^2$, with mean $\mu = \langle n_l \rangle$ and variance $\sigma^2 = \langle n_l^2 \rangle - \mu^2$, accounts for the large part of the optimal sensitivity found (it is even exact for the case $U = 0$). Nevertheless, the genuinely non-Gaussian part of the photon number statistics is crucial to explain the actual advantage seen for deep circuits with a nonzero gate nonlinearity $U\Delta t$.

Finally, in Fig. 7(c), the design of an optimal circuit is illustrated for the case $L = 5$, $D = 16$ and $U\Delta t = 0.08$, the optimum of the red curve in Fig. 7(b). As can be seen, there is no immediate discernible pattern found in the optimal coupler values $J_{l,d}^{(\text{opt})}$, which are, overall, rather high and close to maximal coupling $\frac{\pi}{4} \approx 0.78$.

From experience, We noticed that the convergence of the FOM (Eq. (26)) depends crucially on the initial condition given to the couplers. When $J^{(\text{init})}$ (set uniform across circuit) is too low, the gradient vanishes due to the exponentially damped connection between the phase-shifted input ($l = 0$) and analyzed output ($l = L - 1$), resulting in an exponentially slow convergence. This is an issue that could be understood from the more general perspective of *barren plateaus* in variational quantum computing [73].

In Appendix F, we study the FI associated with standard homodyne detection schemes, using one linear beam splitter. For the homodyne phase detection of a signal α_s using a local os-

cillator α_{LO} , with $|\alpha_s| = |\alpha_{\text{LO}}| = 1$, we derive that $\text{FI}(\theta) = 1$, with an additional gain of a factor 2 when both outputs are observed simultaneously. In this regime of low photon occupation, we demonstrate in Fig. 7(b) that a significant benefit can be achieved by using a qPIC with multiple waveguides (which serve as local oscillators) and a stacked pattern of nonlinear gate interferences; this leads to values of FI well above the values reachable with homodyne detection.

To conclude this part, we presented a procedure for optimizing the qPIC phase readout capability in the limit of low photon occupation by analyzing the photon number distribution P_n of one output signal. It was found that, while multiple linear photonic interferences provide a significant benefit over standard homodyne detection for the extraction of FI, adding modest circuit gate nonlinearities $0 < U \cdot \Delta t \lesssim 0.1$ can provide an additional improvement. This is not fully understood by solely considering the Gaussian statistics of the output light, but requires a perception of the full quantum photon number statistics.

In the future, more generally, both a stage of state preparation and of state readout can be optimized for the maximizing the qPIC phase-sensing potential, as explained in Ref. [57]. Recently, this was studied for two-mode photonic circuits in Ref. [71], using a Kerr-type nonlinearity, and this can be generalized to larger qPICs.

6 Conclusions and outlook

We developed a method for qPIC design optimization in the low-photon occupation regime, enabling the capture of quantum statistics throughout the optimization process. This was achieved by deploying a differentiable tensor-network representation of the bosonic field of a photon pulse in the qPIC waveguides, thus allowing for (i) efficient unitary circuit contraction with the possibility to include non-unitary loss channels for the evaluation of the figure of merit and (ii) gradient tracking for optimizing the qPIC design. Starting from classical field equations, we established a mapping to a design-level description of photonic quantum circuits, thereby providing a practical framework for the optimization of qPICs. Photonic losses can be incorporated during the optimization, using Monte

Carlo sampling methods encoded in dissipative single-mode loss gates which preserve the differentiable nature of the tensor contraction. The method was put in practice for three use-cases: in the realm of quantum state preparation, unitary qPIC odd cat-state generation and noisy single-photon generation were considered, and for quantum sensing, the optimal qPIC sensitivity was achieved by reading out the photon number distribution. For cat-state generation, we found that the circuit-accumulated nonlinearity, combined with sufficient iterations of three-waveguide nonlinear interference suffices for high-fidelity and high-probability success outcomes. For single-photon generation, the dissipation induced by strongly coupling the light to the excitonic degree of freedom was explicitly incorporated in the optimization procedure, using Monte Carlo sampling techniques, to maximize the generation of strong antibunched photon statistics, while simultaneously maximizing output intensity. We concluded that, while the degree of antibunching primarily depends on the circuit-accumulated nonlinearity, subdivisions in more circuit layers lead to slightly higher probabilities of single-photon generation. Finally, we demonstrated the case of optimal readout of quantum sensing by maximizing the circuit sensitivity towards a small phase shift of the incoming coherent light. We found that deep qPICs can potentially offer a significant benefit for the Fisher information extracted by analyzing the output photon number distribution. The multimode qPIC photonic interferences result in a significant improvement over standard homodyne methods. Moreover, a nonzero photonic nonlinearity leads to genuine non-Gaussian photon statistics of the output signal, which, in turn, can effectuate an additional benefit over linear multimode processing.

The proposed optimization scheme for qPICs can also be extended to enhance several other contemporary use cases in quantum processing. To support broader adoption, we have open-sourced the developed code in [32]. As a first continuation, quantum phase sensing and metrology can be further improved and finetuned. As of now, we presented an optimal phase-sensing readout scheme for coherent light, but, more generally, the two stages of state initialization and state readout can be optimized for maximizing

the multimode phase sensitivity [59, 71]. The simultaneous optimization of both may lead to an enhanced scheme, in which the advantage of the multimode nature of the quantum light is maximally profited from when extracting the Fisher information from qPIC readout, thereby breaching scaling limits from classical signal detection. Second, while we showed a brief analysis of the circuit robustness for cat-state generation (see Appendix D), this can be expanded in future works and should be explicitly considered for any real-world use case. To this end, in classical integrated photonics, several methods exist to perform noise-aware optimization of a certain processing tasks – see, e.g., Ref. [16, 53]. In addition to that, also the sparsity of the circuit can be optimized further to limit the impact of fabrication errors in the final detection. Moreover, we now only analyzed the possibilities of coherent light as input, with the conditioning of nonzero output signal, but this can be further expanded. For example, considering single-photon input in one or more waveguides, or conditioning output state-generation of one waveguide on the detection of single (or multiple) photon clicks in another, provide valuable resources for augmenting the quantum nature of the photonic output signal.

In terms of simulation methods, we proposed an optimization scheme based on tensor-network contraction, valid for photonic quantum states in the low occupation regime. The limited set of tensor operations is highly convenient for tracking the gradients towards circuit parameters. Yet, this imposes sharp limits on (i) the photonic Fock space (mode occupation) and (ii) the bipartite entanglement that can be reliably encapsulated. In that sense, for larger photonic mode occupation and intermode entanglement, considering continuous-variable simulation methods could be beneficial for developing the circuit optimization. For example, the positive-P representation [22], recently used for describing quantum optical neural networks [74], does not impose a sharp cut-off on photon occupation, but it faces difficulties, due to the multiplicative noise sampling, in the regime of high occupation, strong nonlinearity and weak dissipation [75]. These challenges must be compared more closely with the ones from the tensor description of the photonic field. Furthermore, in the weakly interacting regime,

approximate variational simulation methods may suffice for developing the qPIC optimization. In that realm, deterministic variational methods in the Gaussian manifold of quantum states (also known as Hartree-Fock-Bogoliubov [76]) can be considered, possibly incorporating higher-order non-Gaussian cumulants [77], or approximate stochastic methods, in particular the truncated Wigner approach [22, 75]. With those methods, much larger circuits can be simulated, using more bosonic modes and gate operations, without inflicting stringent constraints on photonic occupation or multimode entanglement statistics. Nevertheless, this comes at the cost of capturing only a limited and well-contained part of the inherent photon statistics that designate the photonic quantum nature of light. To finish, while we illuminated GaAs-based planar samples as the baseline for the present work, a plethora of different materials and coupling mechanisms can be explored for integration in photonic architectures. Recently, 2D materials are gaining ample interest for devising strong coupling to light. Furthermore, vibrational couplings (Raman modes), plasmonics or coupled chains of cavity systems are amongst the possibilities for further exploration and characterization.

Acknowledgements

We thank Wolfer Peelaers for insightful discussions and a careful reading of the manuscript. We are also grateful to Michiel Wouters for valuable input, particularly on polaritonics, and to Luis Pedro Garcia-Pintos for his contributions

on quantum sensing, both of whom also carefully read the manuscript. We further acknowledge our partners in the project “Quantum Optical Networks based on Exciton-polaritons” (Q-ONE) for stimulating discussions during the development of this work. This project has received funding from the European Union’s EIC Horizon Europe Pathfinder Challenges program under grant agreement No. 101115575 (Q-ONE). The views and opinions expressed are those of the authors only and do not necessarily reflect those of the European Union, the European Innovation Council, or the SMEs Executive Agency (EISMEA). Neither the European Union nor the granting authority can be held responsible for them.

A Deriving the gate dynamics of the qPIC from full 2D field simulations

We work out a blueprint for the gate composition achievable in GaAs-based photonic integrated circuit using simulations of the full 2D polaritonic field, defined in the plane in which the waveguide circuit topology is etched. A short introduction is given to describe the method.

A.1 The 2D field equations

The 2D Hamiltonian for the chip is expressed in terms of the bosonic photon field operators $\hat{\psi}_{\text{ph}}(\mathbf{r})$ and $\hat{\psi}_{\text{ex}}(\mathbf{r})$ for the photons and excitons, respectively,

$$\hat{\mathcal{H}} = \hat{\mathcal{H}}_{\text{ph-ex}} + \hat{\mathcal{H}}_{\text{int}} + \hat{\mathcal{H}}_{\text{pot}}. \quad (27)$$

The first term gives the photon and exciton dispersion and the photon-exciton coupling,

$$\hat{\mathcal{H}}_{\text{ph-ex}} = \int d^2\mathbf{k} \left[\hbar\omega_{\text{ph}}(\mathbf{k})\hat{a}_{\text{ph}}^\dagger(\mathbf{k})\hat{a}_{\text{ph}}(\mathbf{k}) + \epsilon(\mathbf{k})\hat{a}_{\text{ex}}^\dagger(\mathbf{k})\hat{a}_{\text{ex}}(\mathbf{k}) \right] + \frac{\hbar\Omega_R}{2} \int d^2\mathbf{k} \left[\hat{a}_{\text{ph}}^\dagger(\mathbf{k})\hat{a}_{\text{ex}}(\mathbf{k}) + \hat{a}_{\text{ex}}^\dagger(\mathbf{k})\hat{a}_{\text{ph}}(\mathbf{k}) \right]. \quad (28)$$

Here, $\hat{\psi}_{\text{ph,ex}}(\mathbf{r}) = 1/\sqrt{V} \int d^2\mathbf{k} e^{i\mathbf{r}\cdot\mathbf{k}} \hat{a}_{\text{ph,ex}}(\mathbf{k})$ is the Fourier transform of the photon (ph) or exciton (ex) field. The first term in (28) represents the bare in-plane photon dispersion $\omega_{\text{ph}}(\mathbf{k})$ and exciton dispersion $\epsilon(\mathbf{k})$. We assume the photon dispersion to be effectively linear, that is $\omega_{\text{ph}}(\mathbf{k}) = c_{\text{eff}}|k|$, with $c_{\text{eff}} = c/n$ the speed of light in the material (c the speed of light in vacuum and n the relative refractive index of the material), while the exciton dispersion is constant,

$\epsilon(\mathbf{k}) = \hbar\omega_{\text{ex}}$, as it represents (largely) immobile massive excitons, with negligible dispersion as compared to relevant photonic energies. The second term in Eq. (28) describes the exciton-photon coupling in the strong coupling regime, given by the Rabi frequency Ω_R [5]. For maximal in-plane coupling, we assume the photonic field to be in transverse magnetic (TM) zero eigenmode [37], so that only one polarization component of the exciton and photon field is considered.

The second term in Eq. (27) describes the local exciton-exciton interaction,

$$\hat{\mathcal{H}}_{\text{int}} = \frac{g_{2D}}{2} \int d^2\mathbf{r} \, \hat{\psi}_{\text{ex}}^\dagger(\mathbf{r}) \hat{\psi}_{\text{ex}}^\dagger(\mathbf{r}) \hat{\psi}_{\text{ex}}(\mathbf{r}) \hat{\psi}_{\text{ex}}(\mathbf{r}), \quad (29)$$

with g_{2D} the 2D interaction constant of the contact interaction excitons experience in the plane. Since uniform polarization of the light is considered (indistinguishable photons), a repulsive fermionic exchange interaction is dominant, with $g_{2D} > 0$ [34]. When applying an external electric field, the induced exciton dipole-dipole interaction amplifies the effective interaction strength, possibly several orders of magnitude [1, 2, 3].

Finally, the last term in (27) is the potential experienced by the photons for the transversal confinement in the etched waveguide configuration,

$$\hat{\mathcal{H}}_{\text{pot}} = \int d^2\mathbf{r} \, V_{\text{ph}}(\mathbf{r}) \hat{\psi}_{\text{ph}}^\dagger(\mathbf{r}) \hat{\psi}_{\text{ph}}(\mathbf{r}). \quad (30)$$

The photonic potential $V_{\text{ph}}(\mathbf{r})$ is engineered by etching the 2D GaAs sample, which locally modifies the in-plane effective 2D refractive index experienced by the light (see, e.g., Ref. [2]). This can be understood immediately from the wave equation of the classical photonic field, $\psi_{\text{ph}} = \langle \hat{\psi}_{\text{ph}} \rangle$

$$\nabla^2 \psi_{\text{ph}} - \frac{n^2(\mathbf{r})}{c^2} \partial_t^2 \psi_{\text{ph}} = 0, \quad (31)$$

$$\omega_{\text{UP,LP}}(\mathbf{k}) = \frac{1}{2} \left((\omega_{\text{ph}}(\mathbf{k}) + \omega_{\text{ex}}) \pm \sqrt{\Omega_R^2 + (\omega_{\text{ph}}(\mathbf{k}) - \omega_{\text{ex}})^2} \right), \quad (34)$$

with corresponding eigenmodes,

$$\begin{pmatrix} \hat{a}_{\text{ph}}(\mathbf{k}) \\ \hat{a}_{\text{ex}}(\mathbf{k}) \end{pmatrix} = \begin{pmatrix} \cos \theta_{\mathbf{k}} & -\sin \theta_{\mathbf{k}} \\ \sin \theta_{\mathbf{k}} & \cos \theta_{\mathbf{k}} \end{pmatrix} \begin{pmatrix} \hat{a}_{\text{UP}}(\mathbf{k}) \\ \hat{a}_{\text{LP}}(\mathbf{k}) \end{pmatrix}, \quad (35)$$

and $\tan \theta_{\mathbf{k}} = \frac{\Omega_R}{\omega_{\text{ph}}(\mathbf{k}) - \omega_{\text{ex}}}$. In what follows, we assume the incident light is in close resonance with the LP branch, so that the excitation of the

from which the Helmholtz equation follows for monochromatic light, $\psi_{\text{ph}}(\mathbf{r}, t) = \phi(\mathbf{r}) e^{i\omega t}$,

$$\nabla^2 \phi + k_0^2 n^2(\mathbf{r}) \phi = 0, \quad (32)$$

with $k_0 = 2\pi/\lambda = \omega/c$, with λ the wavelength. Comparison with the Schrödinger equation and recalibration of energy tells us that,

$$V(\mathbf{r}) = k_0^2 (n_0^2 - n^2(\mathbf{r})) \approx -2k_0^2 n_0 \Delta n(\mathbf{r}), \quad (33)$$

which holds for $|n_0 - n(\mathbf{r})| \ll n_0$, with n_0 the material refractive index and $n(\mathbf{r}) = n_0 + \Delta n(\mathbf{r})$ the etched index landscape.

The potential to shape the 2D photonic potential landscape by imprinting waveguide designs on the chip is a core component of the research presented in the main text. Identifying and quantifying the effective circuit-gate coupling constant J and nonlinearity U of a gate design under some form of optical excitation will be explored in what follows.

A.2 2D Gross-Pitaevskii gate simulation

The photon-exciton coupling Hamiltonian, $H_{\text{ph-ex}}$ from Eq. (28), is diagonalized in momentum space, which gives the upper (UP) and lower polariton (LP) dispersion [4, 5],

UP branch can be neglected. We restrict to the bosonic operators $\hat{a} := \hat{a}_{\text{LP}}$, with a rescaled lower-polariton potential with $V := V_{\text{pol}} = \sin^2 \theta_{\mathbf{k}} V_{\text{ph}}$ and a LP interaction $g := g_{\text{LP,2D}} = \cos^4 \theta_{\mathbf{k}} g_{2D}$, with $u_{\mathbf{k}}^2 = \cos^2 \theta_{\mathbf{k}}$ the excitonic and $v_{\mathbf{k}}^2 = \sin^2 \theta_{\mathbf{k}}$ photonic fraction [5].

Following this, we find an effective model that describes the dynamics of the LP field $\psi(\mathbf{r}, t) := \langle \psi_{\text{LP}}(\mathbf{r}, t) \rangle$ on the level of mean-field dynamics,

$$i\partial_t \psi(\mathbf{r}, t) = -i\gamma(\mathbf{r}) \psi(\mathbf{r}, t) + \mathcal{E}[\psi(\mathbf{r}, t)] + g|\psi(\mathbf{r}, t)|^2 \psi(\mathbf{r}, t) + V(\mathbf{r})\psi(\mathbf{r}, t). \quad (36)$$

Here, in general, a space-dependent polaritonic loss rate $\gamma(\mathbf{r})$ is added.

The dispersion experienced by the photons is approximated. The light is injected along z -

direction, at narrow linewidth and in close resonance with the exciton level. The direction x , transverse to the propagation, is where the waveguide confinement takes place, with a length scale of the same order as the wavelength of the light. Therefore, the light has a broad spectral range in the x direction. Under these considerations, we assume the polaritonic dispersion to be,

$$\mathcal{E}(\mathbf{k}) = \sqrt{((c/n_0)k_x)^2 + (v_g k_z)^2}, \quad (37)$$

where $v_g = \frac{\partial \omega_{\text{LP}}(k_z)}{\partial k_z}$ is the LP group velocity that represents the field propagation in z -direction, under strong resonant coupling to the exciton mode. For now, we neglect the dispersive curvature – that is, it is assumed that the photonic field linewidth is sufficiently narrow as compared to the dispersive curvature. Similarly, we also neglect the \mathbf{k} -dependence of the LP nonlinearity g . In x direction, in contrast, the light is broadband due to the transverse waveguide confinement and we can neglect the excitonic coupling, so that only the photonic linear dispersion (material speed of light c/n_0) matters. We consider the case $\gamma(\mathbf{r}) = 0$ – no polaritonic losses are included in the simulations.

Eq. (36) is efficiently solved using the split-step method, where each differential time step the interaction and potential term are evaluated in real-space, while the dispersion $\mathcal{E}(\mathbf{k})$ is applied to the Fourier modes, obtained after a 2D fast Fourier transform (FFT).

A.3 Results of 2D simulation

We present the results of a 2D planar field simulation in Fig. 8. The parameters used for the simulation are based on GaAs 2D planar heterostructures. In summary, we used 780 nm input light, injected in waveguides of width $0.5 \mu\text{m}$, with coupling length of $50 \mu\text{m}$, at $0.5 \mu\text{m}$ separation. The in-plane refractive index of the 2D sample is set to $n_0 = 3.28$, valid for a 2D stack of GaAs (quantum well) and AlGaAs layers (cladding) at cryogenic temperatures in the near-infrared regime, and we set $\Delta n = 0.1$, realized by the etching in the cladding. The pulse duration is $\sigma_t = 1 \text{ ps}$ and it contains an average of $\mathcal{N} = 10$ photons, injected in the lowest transverse eigenmode of the waveguide potential (TM₀-mode). The nonlinearity was set to $g = 600 \mu\text{eV} \cdot \mu\text{m}^2$, in accordance with Ref. [3]. Finally, the LP group velocity

was $v_g = 0.5 \cdot c/n_0$, so a factor 2 lower than the photonic velocity, due to the strong excitonic coupling of the light. This corresponds to an exciton fraction of $u_k^2 = 0.5$.

In Fig. 8(a), time slices of the simulation are shown, while Fig. 8(b) shows the calculated 1D waveguide field, obtained by integrating over the transverse direction $x < 0$ (left waveguide) or $x > 0$ (right waveguide). By comparison with the same simulation for a linear coupler, that is, with $g = 0 \mu\text{eV} \cdot \mu\text{m}^2$, we can identify the parameters that define this gate – a linear coupling ratio of 0.72, meaning $\theta = J\Delta t = 0.68\pi$, and a gate accumulated nonlinearity phase shift of $\theta_0^{(\text{nl})} = 0.14\pi$ on the left side and $\theta_1^{(\text{nl})} = 0.11\pi$ on the right. This was obtained for a gate extent of $400 \mu\text{m}$ and a time $t_{\text{end}} = 8.31 \text{ ps}$. For realizing the coupling, a gate length of $100 \mu\text{m}$ is sufficient, in line with the parameter estimate at the end of Sec. 4.1 of the main text.

The gate nonlinearity rate U can be evaluated from the injected normalized pulse field intensity,

$$n(\mathbf{r}) = \frac{1}{\sqrt{2\pi}\sigma_z} \exp\left\{-\frac{(z-z_0)^2}{4\sigma_z^2}\right\} \times \mathcal{F}_{\text{tr}}(x), \quad (38)$$

with $\sigma_z = v_g \sigma_t$ the spatial pulse extent and $\mathcal{F}_{\text{tr}}(x)$ the transverse confined eigenmode of the waveguide. From this we find,

$$U = \int_{\mathbf{r}} d^2r n(\mathbf{r}) [g n(\mathbf{r})] =: \frac{g}{S_{\text{pulse}}} \quad (39)$$

Using the parameters of simulation, we find a gate nonlinearity of $U = 0.0065 \text{ ps}^{-1}$ and effective pulse surface $S_{\text{pulse}} = 141 \mu\text{m}^2$, so that $U\Delta t = 0.013$, for a $100 \mu\text{m}$ gate. Note that this can be further improved with a slower group velocity v_g ; this will both extend the exposure time to the nonlinearity and contract the incoming pulse stronger in the direction of propagation. Therefore, a factor 4 in reduction of v_g , will yield a factor 16 of improvement for $U\Delta t$. This would bring us into the regime considered for, e.g., the case of cat-state optimization in Sec. 4.1, where values up to $U\Delta t$ were considered for $> 100 \mu\text{m}$ gate structures. This could be achieved in experiment by exciting at high exciton fraction [36] and using techniques of slow light [38].

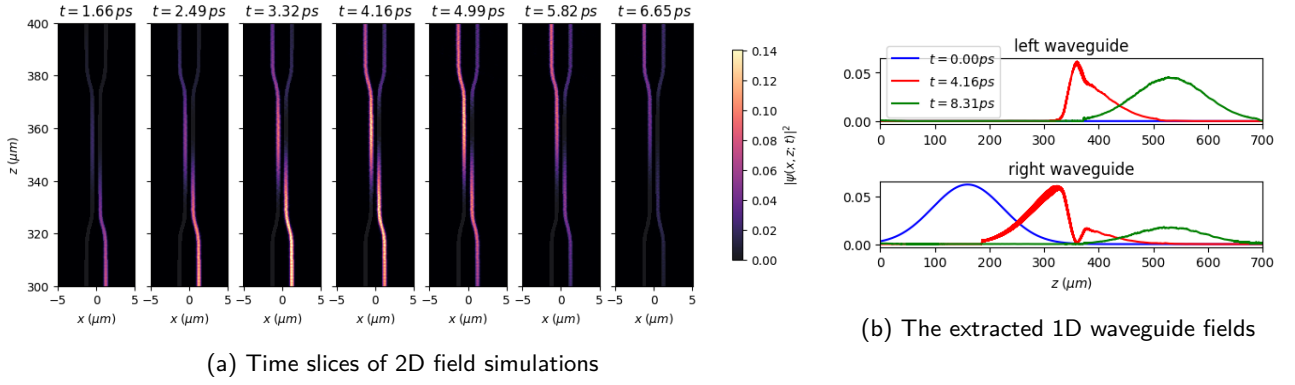


Figure 8: Results of 2D LP field simulations of one nonlinear gate, with $50 \mu\text{m}$ coupling. (a) Time slices of the 2D field density as the photon pulse propagates through. (b) The waveguide 1D field occupations at the initial (blue), middle (red) and final (green) simulated time steps, obtained by integrating over the x direction.

B Deriving the gate parameters under pulsed laser excitation

For the purpose of estimating more carefully the parameters that define the gates, we reduce the

full 2D waveguide field simulation from Appendix A to a set of two coupled 1D equations, with effective coupling $J_{i,i\pm 1}$ between neighboring waveguides,

$$i(\partial_t + v_g \partial_z) \psi_i(z, t) = g_{1D} |\psi_i(z, t)|^2 \psi_i(z, t) - J_{i-1,i}(z, t) \psi_{i-1}(z, t) - J_{i,i+1}^*(z, t) \psi_{i+1}(z, t). \quad (40)$$

Here, $\psi_i(z, t) = \langle \psi_{\text{LP},i}(z, t) \rangle$ is the LP field in waveguide i at time t and position z in the waveguide and v_g the LP group velocity. The couplings $J_{i,i\pm 1}(z, t)$ describe the tunneling rates between two adjacent waveguides, as can be estimated, to first order, from the waveguide TM_0 -mode profile overlap [29]. However, more accurate values can be obtained with a simulation of the full 2D gate architecture in the linear regime, as was presented in Appendix A.

The parameter g_{1D} is the 1D polariton interaction constant, which is found from g by integrating out the transversal dimension of waveguide confinement,

$$g_{1D}(z) = g \int dx n(x, z)^2, \quad (41)$$

with $n(x, z)$ the normalized pulse shape from Eq. (38). We set $g_{1D}(z) = g_{1D}$ in the simulation, thus again neglecting dispersive curvature for the pulse propagation.

A pulse of Gaussian shape, containing an average of $\mathcal{N} = 10$ photons, is injected in the first waveguide ($i = 0$) at position z_0 and width

$\sigma_z = v_g \sigma_t$, with σ_t the pulse duration,

$$\psi_0(z, t = 0) = \sqrt{\frac{\mathcal{N}}{\sqrt{2\pi}\sigma}} \times e^{ik_z z} \times \exp\left\{-\frac{(z - z_0)^2}{4\sigma_z^2}\right\}. \quad (42)$$

The wavevector $k_z = n_0 k_0$, with n_0 the effective 1D refractive index and $k_0 = 2\pi/\lambda$, with λ the wavelength – $\lambda = 780 \text{ nm}$ for exciton resonance in GaAs.

Starting from the pulse 1D field dynamics, the goal is to establish a photonic circuit model of the form,

$$i\partial_t \alpha_0 = -J\alpha_1 + U|\alpha_0|^2 \alpha_0, \quad (43)$$

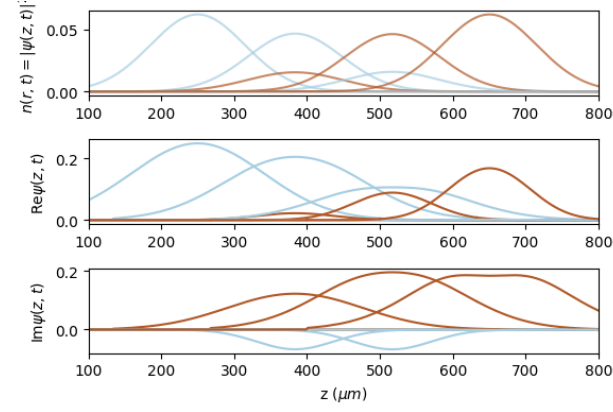
$$i\partial_t \alpha_1 = -J\alpha_0 + U|\alpha_1|^2 \alpha_1. \quad (44)$$

Here, α_i are bosonic field modes that describe the photonic component of the pulse. Furthermore, J is the linear coupling between the modes and U is the photonic nonlinearity, both expressed as temporal rates (inverse time units).

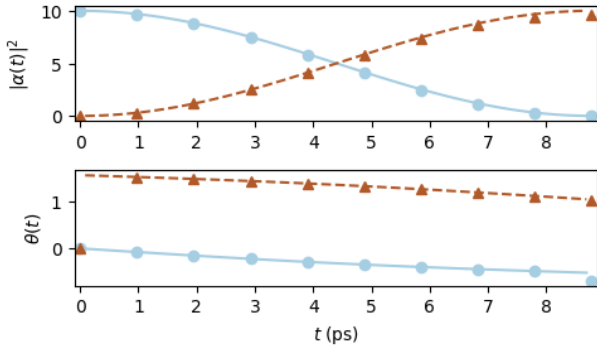
The normalized 1D field pulse profile at incidence,

$$w(z, t = 0) = \frac{1}{\sqrt{\mathcal{N}}} \psi_0(z, t = 0), \quad (45)$$

serves as a reference for obtaining the bosonic circuit modes by evaluating the field overlap at



(a) Snapshots of the pulse propagating from left to right, at 2.93 ps apart



(b) Comparing the 1D field dynamics (points) with the a circuit gate model (lines)

Figure 9: The propagation of a pulse through a $\pi/2$ swap gate with a strong photonic nonlinearity. The pulse is injected in first waveguide (blue) and transfers to the second (brown) (a) different snapshots, $\Delta t = 2.93$ ps apart from each other, of the pulse propagating through the coupled waveguides from left to right; the photon density (up), and the real (middle) and imaginary part (bottom) of $\psi_{0,1}(z, t)$. (b) The mapping to an effective circuit model, using the circuit coupling J and nonlinearity U . The values from the circuit simulation (full and dashed lines) are compared with the values extracted from the field simulation (dots and triangles), same color codes as (a).

later times t , in waveguide l ,

$$\alpha_l(t) = \int_{-\infty}^{\infty} dz w(z, t=0) \psi_i(z, t). \quad (46)$$

The circuit nonlinearity is derived similarly as for the 2D case (39),

$$U = g_{1D} \int_{-\infty}^{\infty} dz |w(z, t=0)|^4. \quad (47)$$

As explained above for the 2D case, the circuit nonlinearity U can be changed by changing the pulse duration $\sigma_t = \sigma_z/v_g$ (see Eq. (42)); shorter pulses give higher U .

In Fig. 9, we show the simulation of two coupled waveguides (Fig. 9(a)) and the corresponding mapping to circuit gate model (43) (Fig. 9(b)), in a regime of relatively strong nonlinearity, $g_{1D} = 1200 \mu\text{eV} \cdot \mu\text{m}$, similar to what was reported in [3] in case of $\sim 0.5 \mu\text{m}$ transverse waveguide confinement – see parameters used in Appendix A. The linear gate coupling was set to represent a swap gate, $J\Delta t = \pi/2$, with Δt the time of integration, and the pulse has a duration set to $\sigma_t = 1$ ps, containing on average $\mathcal{N} = 10$ photons. The LP group velocity was set to $v_g = 45.58 \mu\text{m} \cdot \text{ps}^{-1}$, corresponding to a reduction factor of about 2 as compared to bare GaAs-based samples due to the exciton coupling (LP exciton fraction $u_k^2 \approx 0.5$, see Eq. (35) and below); this is in line with values reported in Ref. [36]. The waveguide dynamics is shown in Fig. 9(a), where it is seen that the nonlinearity causes, in the first place, intensity-dependent phase shifts. In Fig. 9(b), a comparison with the mapping to circuit gate dynamics from Eqs. (43) is shown, using the bosonic field modes $\alpha_i(t)$ defined in Eq. (46). We derive an effective gate nonlinearity of $U = 0.013 \text{ ps}^{-1}$ or, in length units, $U/v_g = 0.38 \text{ mm}^{-1}$. Consequently, for a gate design of, e.g., $500 \mu\text{m}$, we would find a dimensionless value of $U\Delta t \approx 0.2$.

In 9(b), the interaction-induced phase shift that develops over time in the 1D field simulation of the pulses (dots and triangles) is in good agreement with the effective circuit simulation. However, when considering this regime of very strong photonic nonlinearity, small deviations start showing up at long times. This is attributed to the strong nonlinearity g_{1D} and a high number of $\mathcal{N} = 10$ photons per pulse, which causes in-pulse phase fluctuations (see final time slice 9(a)) and therefore slightly affects the accuracy of the overlap integral from Eq. 46.

C Quantum Fisher information in coherent input state

The quantum Fisher information (QFI) is defined as,

$$\text{QFI}(\theta) = 4 \cdot \lim_{\theta \rightarrow 0} \frac{1 - \mathcal{F}[\rho(0), \rho(\theta)]}{\theta^2}, \quad (48)$$

with,

$$\mathcal{F}[\rho_1, \rho_2] = \left(\text{Tr} \sqrt{\sqrt{\rho_1} \rho_2 \sqrt{\rho_1}} \right)^2, \quad (49)$$

the quantum Uhlmann fidelity between the unperturbed state $\rho(0)$ and the perturbed $\rho(\theta)$, which has a small phase shift θ . It provides the maximal classical Fisher information that can be obtained from the measurement statistics of an optimal Hermitian observable B [60],

$$\text{QFI}(\theta) = \sup_B \text{FI}(\theta|B), \quad (50)$$

with,

$$\text{FI}(\theta|B) = \sum_b P_b(\theta|B) \times (\partial_\theta \log P_b(\theta|B))^2, \quad (51)$$

where $P_b(\theta|B) = \langle b|\rho(\theta)|b\rangle$ are the classical probabilities of the measurement outcome b of the Hermitian operator B , i.e., the eigenmodes $B|b\rangle = b|b\rangle$.

For the use case of quantum phase sensing considered in Sec. 5, a small phase shift was given to one circuit input mode, as expressed in Eq. (6) from main text. The QFI is obtained from the overlap between the unperturbed and perturbed state,

$$\begin{aligned} \mathcal{F}[\rho^{(l)}(\theta), \rho^{(l)}(0)] &= |\langle \alpha e^{i\theta} | \alpha \rangle|^2 \\ &= e^{-|\alpha|^2 |e^{i\theta} - 1|^2} \\ &= 1 - |\alpha|^2 \theta^2 + \mathcal{O}(\theta^4) \end{aligned} \quad (52)$$

Hence, from Eq. (48), we find the quantum Fisher information contained in a phase-shifted coherent state to be $\text{QFI} = 4|\alpha|^2$, directly proportional to the coherent photon intensity $|\alpha|^2$.

D Circuit robustness for odd cat state preparation

After establishing an optimal qPIC configuration for some optimization task, it is important to analyze the robustness and stability of the qPIC towards small fabrication errors and measurement inaccuracies. In this appendix, we perform a circuit robustness analysis for odd cat-state preparation, as outlined in Sec. 4.1, towards fabrication errors in the gate couplings, e.g., caused by small imperfections in etched waveguide gate separation.

For this study, we added multiplicative noise to the optimal coupling rates $J_{l,d}^{(\text{opt})}$, obtained after optimization,

$$\tilde{J}_{l,d}^{(b)} \leftarrow J_{l,d}^{(\text{opt})} (1 + \sigma \xi_{l,d}^{(b)}), \quad (53)$$

with σ the variance and $\xi_{l,d}^{(b)} \sim \mathcal{N}(0, 1)$ normal-distributed random noise, the index b labels the sample set. Importantly, the fabrication noise is considered multiplicative; a small separation mismatch for two waveguides close to each other, corresponding to strong couplers $J_{l,d}^{(\text{opt})}$, will have a much larger impact than two waveguides far away, as they have (almost) zero coupling.

In Fig. 10, we show the results for different levels of noise in the couplers (logarithmic scale), for deep circuits $D = 25$ and a circuit nonlinearity $U \cdot T_{\text{circ}} = 6.25$. We studied the robustness for $L = 3$ and $L = 11$ waveguides, which showed similar outcomes for fidelity after optimization in the text – see Fig. 5(e)-(f). The box of each data point was generated with 100 different random samples b , as defined in Eq. (53). Here again, there is no compelling evidence found for preferring larger circuits, with $L = 11$, over smaller, with $L = 3$, when considering their robustness. We see that odd cat-state generation is relatively stable towards fabrication errors in the gate couplings up to relative errors $\sigma \approx 10\%$; this results in a loss of 2 – 3% in average fidelity and an increase in spread (interquartile range) of about 8%, excluding outliers.

In summary, we performed an analysis of the circuit robustness towards fabrication errors in the couplers $J_{l,d}$ of qPIC optimized for odd cat-state generation. In the future, also detector noise, especially important for evaluating the photonic Fisher information, can be included in the robustness analysis, as well as imperfections related to in- and out-scattering of the qPIC. Furthermore, qPIC robustness can be incorporated as explicit requirement during the optimization, as was considered, for example, in Refs. [17, 53, 16] for neuromorphic computing. After outlining the relevant noise channels for a specific qPIC task, similar methods can be used in the tensor-network simulations.

E Gaussian quantum state sensing

In the main text, Sec. 5, a qPIC optimization scheme was developed for optimal phase-shift

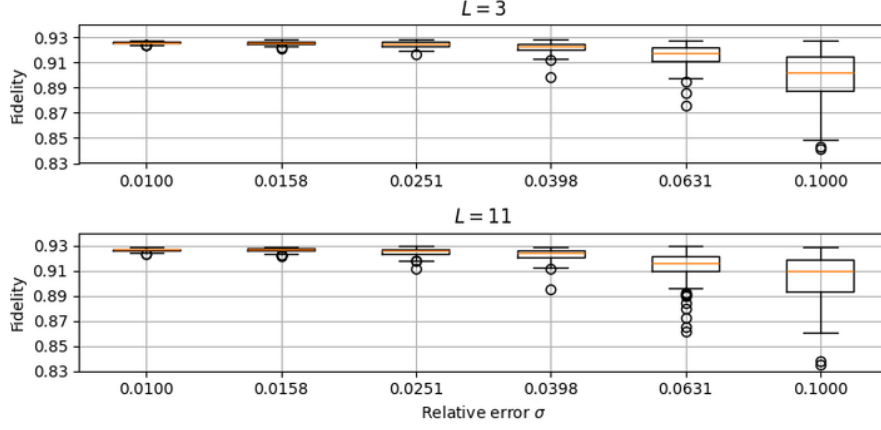


Figure 10: The robustness analysis for cat-state generation with deep circuits, $D = 25$ and $U \cdot T_{\text{circ}} = 6.25$, for $L = 3$ (top) and $L = 11$ (bottom) coupled waveguides, using boxplots.

sensing, based on detecting the photon number distribution of the one output mode. Here, we explain that, to some extent, the extraction of information from the circuit can be understood from Gaussian sampling methods. For this, we investigate the circuit sensitivity by means of the Gaussian Fisher Information (GFI),

$$\text{GFI} := \frac{1}{\sigma^2} \left(\frac{\partial \mu}{\partial \theta} \right)^2, \quad (54)$$

with, in the case of qPIC output signal sampling, the mean output of mode l , $\mu = \langle n_l \rangle$, and the variance, $\sigma^2 = \langle n_l^2 \rangle - \mu^2$. This coincides with standard formulation of Fisher information contained in Gaussian distributions, on the condition that $\frac{\partial \sigma^2}{\partial \theta}$ is negligible – see, e.g., Ref. [72].

In Fig. 11, we present the results of the analysis. Fig. 11(a)-(b) show the μ and σ^2 , extracted from the number distribution, for circuits of $L = 5$ waveguides and circuit time $T_{\text{circ}} = D \cdot \Delta t$, with $D = 4$ (blue lines) and $D = 16$ (red lines).

In Fig. 11(c)-(d), the standard deviation σ and $\frac{\partial \mu}{\partial \theta}$ are shown, normalized with μ . Here, it is observed that the standard deviation is generally lower for deeper circuits that have the same gate nonlinearity $U\Delta t$, indicating a small amount of amplitude squeezing at higher gate nonlinearity $U\Delta t$ and circuit depth D . In addition to that, the sensitivity of the mean $\frac{\partial \mu}{\partial \theta}$ becomes higher above $U\Delta t \approx 0.04$, but still lower than the linear case $U = 0$.

These two findings are apparent in Fig. 11(e), where GFI is shown (dotted lines) and compared with the actual FI reached after qPIC optimization (Fig. 7(b), main text). Interestingly, for

$U = 0$, linear qPICs, all points coincide. That is, the FI extracted from the readout of one mode's photon number distribution $P_n^{(l)}$ is equivalent to the Gaussian FI, independent of circuit time $T_{\text{circ}} = D \cdot \Delta t$. This changes for higher $U\Delta t$; shallow circuits show an immediate decline in FI, due to initial effects of blockade, thus affecting the GFI that can be extracted from the output. When analyzing the full number distribution $P_n^{(l)}$, as in the main text, a much slower decline is observed (blue dotted line), which we attribute to the non-Gaussian nature of the photon statistics. In the case of a deep circuit with $D = 16$, this changes somewhat. At higher nonlinearity $U\Delta t$, the GFI declines as well, but much slower than the case $D = 4$, due to the stronger potential to exploit the multimode interferences. As we found in main text, the number-distribution FI contained in P_n slowly increases for small $U\Delta t$ and finds a maximum at $U\Delta t = 0.08$, before it declines again. Therefore, adding non-Gaussian elements in the statistics is, in the analysis of the Fisher information associated with number-resolved measurements, essential to observe the actual advantage of the qPIC compared to a PIC (linear qPIC).

It must be noted that, in the main text, the optimization was carried out for the FI defined on the full photon number distribution $P_n^{(l)}$ as explicit FOM – see Eq. (24). When, on the other hand, the GFI itself is set as the FOM for optimization, this observation could change. Optimization schemes based on the Gaussian form for the FI, defined in Eq. (54) can be investigated in the future – also motivated by the fact that

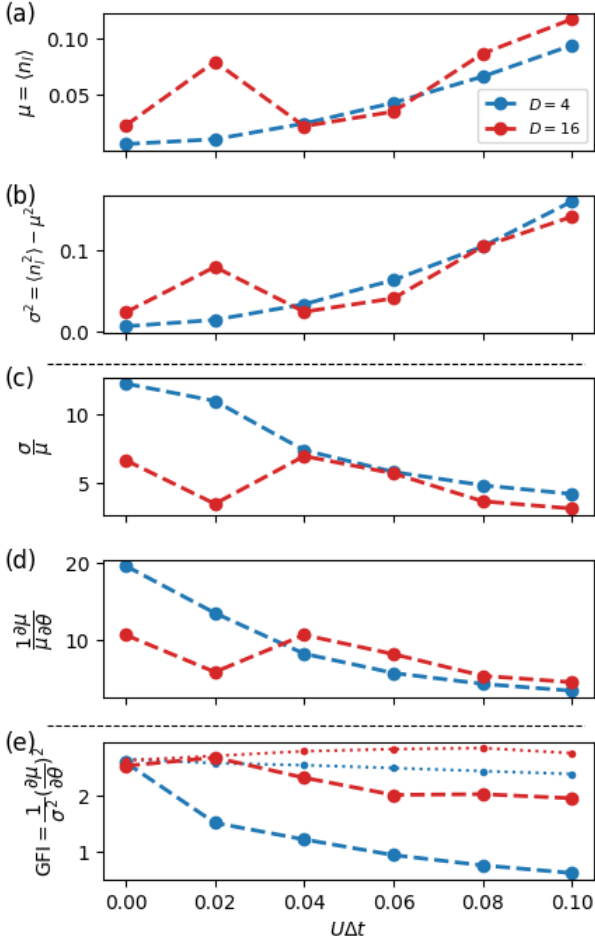


Figure 11: The Gaussian comparison for sensing, for $L = 5$ waveguides, with $D = 4$ (blue) and $D = 16$ (red) circuit layers. (a) the mean photon number and (b) number the variance. (c) The variance σ normalized with μ becomes lower for higher gate nonlinearity $U\Delta t$ and (d) the mean derivative towards θ , normalized with μ , both characterizing the output sensitivity. (e) The Gaussian Fisher information extracted for the experiment (dashed line), compared with the full Fisher information obtained after optimization in main text (dotted). While Gaussian FI contains a large part of the FI, the non-Gaussian statistics of the light are crucial for achieving a benefit over the classical linear case ($U\Delta t = 0$).

this quantity would be more directly accessible in real-world experiments.

Furthermore, we see in Fig. 11(a) that the signal intensity μ for optimal FI extraction becomes very low in the limit of small $U\Delta t$; $\mu = 0.007$

and $\mu = 0.023$, for $D = 4$ and $D = 16$, respectively, at $U = 0$. By solely optimizing the FI *an sich*, we see that the signal intensity already grows up to $\mu \approx 0.1$ for $U\Delta t = 0.1$. Beyond that, also the signal intensity can be added explicitly in the FOM to avoid the decline in signal strength in the circuit output, which might affect the signal-to-noise ratio in experiment. This is similar to what was done for single-photon generation in Sec. 4.3 and can be realized, e.g., by adding a term $\mathcal{L}_{\text{signal}} \propto -\langle n_l \rangle$ in the FOM for sensing defined in Eq. (26).

F Homodyne readout limit for phase sensing

The standard method for obtaining phase information from a photonic signal (classical or quantum) is homodyne detection, using one single linear beam splitter to interfere the signal with a reference beam (a local oscillator).

Generally, the output of one end of the beam splitter is given by,

$$\beta = c\alpha_s + e^{i\phi}\sqrt{1-c^2}\alpha_{LO} \quad (55)$$

$$= c|\alpha_s|e^{i\theta} + e^{i\phi}\sqrt{1-c^2}|\alpha_{LO}| \quad (56)$$

with α_s the phase-shifted signal to be analyzed, α_{LO} the local oscillator, serving as reference, and c^2 is the mixing ratio and ϕ the relative phase. In the second step, it is assumed that α_s and α_{LO} are in phase, up to a small phase shift θ (global phase shifts do not matter).

The absence of photonic nonlinearities implies that the output signal of the beam splitter preserves the coherent Poisson photon-number statistics. For a Poisson distribution with mean μ , the Fisher information is,

$$\text{PFI}(\theta) = \frac{1}{\mu} \left(\frac{\partial \mu}{\partial \theta} \right)^2, \quad (57)$$

equivalent to Eq. (54), if $\sigma^2 \equiv \mu$, as holds for Poissonian statistics.

In our case, the mean μ is given by the signal intensity, so $\mu \equiv |\beta|^2$. Straightforward calculation leads to,

$$\text{PFI}(\theta) \Big|_{\theta=0} = \frac{4 \sin^2(\phi) c^2 (1-c^2) |\alpha_s|^2 |\alpha_{LO}|^2}{c^2 |\alpha_s|^2 + (1-c^2) |\alpha_{LO}|^2 + 2 \cos(\phi) c \sqrt{1-c^2} |\alpha_s| |\alpha_{LO}|} \quad (58)$$

For the case of symmetric beam splitters, the couplers considered in the main text, we have that $\phi = \frac{\pi}{2}$. Furthermore, maximal mixing, $c = 1/\sqrt{2}$ (balanced homodyne measurement), will give optimal results. In this case, we find,

$$\text{PFI}(\theta) = 2 \cdot \frac{|\alpha_s|^2 |\alpha_{LO}|^2}{|\alpha_s|^2 + |\alpha_{LO}|^2}. \quad (59)$$

For the low photonic occupation regime considered in Sec. 5 of main text, $\alpha_s = \alpha_{LO} = 1$, this leads to $\text{PFI}(\theta) = 1$, significantly below the value found after circuit optimization – see Fig. 7 or Fig. 11.

When we consider $|\alpha_{LO}|^2 \gg |\alpha_s|^2$ in Eq. (59), the FI contained in one beam-splitter output converges to $\text{PFI}(\theta) = 2|\alpha_s|^2$, still well below the results found after circuit optimization for reading out one output. Nevertheless, when *both* outputs of the beam splitter are analyzed, with a strong local oscillator α_{LO} , a perfect phase measurement is performed. In that case, an additional factor 2 is gained and the Heisenberg limit, derived in Appendix C, is recovered; $\text{PFI}(\theta) \equiv \text{QFI}(\theta) = 4|\alpha_s|^2$.

References

- [1] SI Tsintzos, A Tzimis, G Stavrinidis, A Trifonov, Z Hatzopoulos, JJ Baumberg, H Ohadi, and PG Savvidis. Electrical tuning of nonlinearities in exciton-polariton condensates. *Physical Review Letters*, 121(3):037401, 2018.
- [2] DG Suárez-Forero, F Riminucci, V Ardizzone, N Karpowicz, E Maggiolini, G Macorini, G Lerario, F Todisco, M De Giorgi, L Dominici, et al. Enhancement of parametric effects in polariton waveguides induced by dipolar interactions. *Physical review letters*, 126(13):137401, 2021.
- [3] Dror Liran, Ronen Rapaport, Jiaqi Hu, Nathaniel Lydick, Hui Deng, and Loren Pfeiffer. Electrically controlled photonic circuits of field-induced dipolaritons with huge nonlinearities. *Physical Review X*, 14(3):031022, 2024.
- [4] J Keeling, FM Marchetti, MH Szymańska, and PB Littlewood. Collective coherence in planar semiconductor microcavities. *Semiconductor science and technology*, 22(5):R1, 2007.
- [5] Iacopo Carusotto and Cristiano Ciuti. Quantum fluids of light. *Reviews of Modern Physics*, 85(1):299–366, 2013.
- [6] Han-Sen Zhong, Hui Wang, Yu-Hao Deng, Ming-Cheng Chen, Li-Chao Peng, Yi-Han Luo, Jian Qin, Dian Wu, Xing Ding, Yi Hu, et al. Quantum computational advantage using photons. *Science*, 370(6523):1460–1463, 2020.
- [7] Valeria Cimini, Mauro Valeri, Simone Piacentini, Francesco Ceccarelli, Giacomo Corrielli, Roberto Osellame, Nicolò Spagnolo, and Fabio Sciarrino. Variational quantum algorithm for experimental photonic multi-parameter estimation. *npj Quantum Information*, 10(1):26, 2024.
- [8] Mohammadjavad Dowran, Aye L Win, Umang Jain, Ashok Kumar, Benjamin J Lawrie, Raphael C Pooser, and Alberto M Marino. Parallel quantum-enhanced sensing. *ACS Photonics*, 11(8):3037–3045, 2024.
- [9] Laura T Knoll, Agustina G Magnoni, and Miguel A Larotonda. Experimental advances in phase estimation with photonic quantum states. *Entropy*, 27(7):712, 2025.
- [10] Joseph Anthony Giordmaine and Robert C Miller. Tunable coherent parametric oscillation in linb o 3 at optical frequencies. *Physical Review Letters*, 14(24):973, 1965.
- [11] R. Paschotta. Optical parametric oscillators. RP Photonics Encyclopedia, 2008. Available online at https://www.rp-photonics.com/optical_parametric_oscillators.html.
- [12] HM Gibbs, Galina Khitrova, and Stephan W Koch. Exciton–polariton light–semiconductor coupling effects. *Nature Photonics*, 5(5):273–273, 2011.
- [13] Aymeric Delteil, Thomas Fink, Anne Schade, Sven Höfling, Christian Schneider, and Ataç İmamoğlu. Towards polariton blockade of confined exciton–polaritons. *Nature materials*, 18(3):219–222, 2019.
- [14] Kevin M Birnbaum, Andreea Boca, Russell Miller, Allen D Boozer, Tracy E Northup, and H Jeff Kimble. Photon blockade in an optical cavity with one trapped atom. *Nature*, 436(7047):87–90, 2005.

- [15] Floris Laporte, Joni Dambre, and Peter Biestman. Highly parallel simulation and optimization of photonic circuits in time and frequency domain based on the deep-learning framework PyTorch. *Sci. Rep.*, 9(1):5918, April 2019.
- [16] Jiaqi Gu, Hanqing Zhu, Chenghao Feng, Zixuan Jiang, Mingjie Liu, Shuhan Zhang, Ray T. Chen, and David Z. Pan. Adept: automatic differentiable design of photonic tensor cores. In *Proceedings of the 59th ACM/IEEE Design Automation Conference, DAC '22*, page 937–942, New York, NY, USA, 2022. Association for Computing Machinery.
- [17] Ziyang Jiang, Pingchuan Ma, Meng Zhang, Rena Huang, and Jiaqi Gu. Adept-z: Zero-shot automated circuit topology search for pareto-optimal photonic tensor cores, 2024.
- [18] Danijela Marković, Alice Mizrahi, Damien Querlioz, and Julie Grollier. Physics for neuromorphic computing. *Nature Reviews Physics*, 2(9):499–510, 2020.
- [19] Nikolay L Kazanskiy, Muhammad A Butt, and Svetlana N Khonina. Optical computing: Status and perspectives. *Nanomaterials*, 12(13):2171, 2022.
- [20] Peter L McMahon. The physics of optical computing. *Nature Reviews Physics*, 5(12):717–734, 2023.
- [21] Francesco Musumeci, Cristina Rottondi, Avishek Nag, Irene Macaluso, Darko Zibar, Marco Ruffini, and Massimo Tornatore. An overview on application of machine learning techniques in optical networks. *IEEE Communications Surveys & Tutorials*, 21(2):1383–1408, 2018.
- [22] Crispin Gardiner and Peter Zoller. *Quantum noise: a handbook of Markovian and non-Markovian quantum stochastic methods with applications to quantum optics*. Springer Science & Business Media, 2004.
- [23] Guifré Vidal. Efficient classical simulation of slightly entangled quantum computations. *Physical review letters*, 91(14):147902, 2003.
- [24] R Dum, AS Parkins, P Zoller, and CW Gardiner. Monte carlo simulation of master equations in quantum optics for vacuum, thermal, and squeezed reservoirs. *Physical Review A*, 46(7):4382, 1992.
- [25] Klaus Mølmer, Yvan Castin, and Jean Dalibard. Monte carlo wave-function method in quantum optics. *JOSA B*, 10(3):524–538, 1993.
- [26] Howard J Carmichael. Quantum trajectory theory for cascaded open systems. *Physical review letters*, 70(15):2273, 1993.
- [27] Andrew J Daley. Quantum trajectories and open many-body quantum systems. *Advances in Physics*, 63(2):77–149, 2014.
- [28] Mathias Van Regemortel, Oles Shtanko, Luis Pedro García-Pintos, Abhinav Deshpande, Hossein Dehghani, Alexey V Gorshkov, and Mohammad Hafezi. Monitoring-induced entanglement entropy and sampling complexity. *Physical Review Research*, 4(3):L032021, 2022.
- [29] Hermann A Haus and Weiping Huang. Coupled-mode theory. *Proceedings of the IEEE*, 79(10):1505–1518, 2002.
- [30] Yufei Xing, Umar Khan, AR Alves Júnior, and Wim Bogaerts. Behavior model for directional coupler. In *Proceedings Symposium IEEE Photonics Society Benelux*, pages 128–131, 2017.
- [31] Shi-Xin Zhang, Jonathan Allcock, Zhou-Quan Wan, Shuo Liu, Jiace Sun, Hao Yu, Xing-Han Yang, Jiezhong Qiu, Zhaofeng Ye, Yu-Qin Chen, et al. Tensorcircuit: a quantum software framework for the nisq era. *Quantum*, 7:912, 2023.
- [32] in preparation.
- [33] F Riminucci, V Ardizzone, L Francaviglia, M Lorenzon, C Stavrakas, S Dhuey, A Schwartzberg, S Zanotti, D Gerace, K Baldwin, et al. Nanostructured gas/(al, ga) as waveguide for low-density polariton condensation from a bound state in the continuum. *Physical Review Applied*, 18(2):024039, 2022.
- [34] Masha Vladimirova, Steeve Cronenberger, Denis Scalbert, KV Kavokin, Audrey Miard, Aristide Lemaître, Jacqueline Bloch, Dimitri Solnyshkov, Guillaume Malpuech, and AV Kavokin. Polariton-polariton interaction constants in microcavities. *Physical*

- [35] Yongbao Sun, Yoseob Yoon, Mark Steger, Gangqiang Liu, Loren N Pfeiffer, Ken West, David W Snoke, and Keith A Nelson. Direct measurement of polariton–polariton interaction strength. *Nature Physics*, 13(9):870–875, 2017.
- [36] PM Walker, L Tinkler, M Durska, DM Whittaker, IJ Luxmoore, B Royall, DN Krizhanovskii, MS Skolnick, I Farrer, and DA Ritchie. Exciton polaritons in semiconductor waveguides. *Applied Physics Letters*, 102(1), 2013.
- [37] Pavel Yu Shapochkin, Maksim S Lozhkin, Ivan A Solovev, Olga A Lozhkina, Yury P Efimov, Sergey A Eliseev, Vyacheslav A Lovcjs, Gleb G Kozlov, Anastasia A Pervishko, Dmitry N Krizhanovskii, et al. Polarization-resolved strong light–matter coupling in planar gaas/algaas waveguides. *Optics Letters*, 43(18):4526–4529, 2018.
- [38] Luis Torrijos-Morán, Amadeu Griol, and Jaime García-Rupérez. Slow light bimodal interferometry in one-dimensional photonic crystal waveguides. *Light: Science & Applications*, 10(1):16, 2021.
- [39] J Ignacio Cirac, David Perez-Garcia, Norbert Schuch, and Frank Verstraete. Matrix product states and projected entangled pair states: Concepts, symmetries, theorems. *Reviews of Modern Physics*, 93(4):045003, 2021.
- [40] David Perez-Garcia, Frank Verstraete, Michael M Wolf, and J Ignacio Cirac. Matrix product state representations. *arXiv preprint quant-ph/0608197*, 2006.
- [41] Johannes Hauschild, Jakob Unfried, Sajan Anand, Bartholomew Andrews, Marcus Bintz, Umberto Borla, Stefan Divic, Markus Drescher, Jan Geiger, Martin Hefel, Kévin Hémerly, Wilhelm Kadow, Jack Kemp, Nico Kirchner, Vincent S. Liu, Gunnar Möller, Daniel Parker, Michael Rader, Anton Romen, Samuel Scalet, Leon Schoonderwoerd, Maximilian Schulz, Tomohiro Soejima, Philipp Thoma, Yantao Wu, Philip Zechmann, Ludwig Zweng, Roger S. K. Mong, Michael P. Zaletel, and Frank Pollmann. Tensor network Python (TeNPy) version 1. *SciPost Phys. Codebases*, page 41, 2024.
- [42] Zhou-Quan Wan and Shi-Xin Zhang. Automatic differentiation for complex valued svd. *arXiv preprint arXiv:1909.02659*, 2019.
- [43] AV Trifonov, SN Korotan, AS Kurdyubov, I Ya Gerlovin, IV Ignatiev, Yu P Efimov, SA Eliseev, VV Petrov, Yu K Dolgikh, VV Ovsyankin, et al. Nontrivial relaxation dynamics of excitons in high-quality ingaas/gaas quantum wells. *Physical Review B*, 91(11):115307, 2015.
- [44] Mathias Van Regemortel, Ze-Pei Cui, Alireza Seif, Hossein Dehghani, and Mohammad Hafezi. Entanglement entropy scaling transition under competing monitoring protocols. *Physical Review Letters*, 126(12):123604, 2021.
- [45] A Paszke. Pytorch: An imperative style, high-performance deep learning library. *arXiv preprint arXiv:1912.01703*, 2019.
- [46] Diederik P Kingma and Jimmy Ba. Adam: A method for stochastic optimization. *arXiv preprint arXiv:1412.6980*, 2014.
- [47] Sanjib Ghosh, Tomasz Paterek, and Timothy CH Liew. Quantum neuromorphic platform for quantum state preparation. *Physical review letters*, 123(26):260404, 2019.
- [48] Sanjib Ghosh, Andrzej Opala, Michał Matuszewski, Tomasz Paterek, and Timothy CH Liew. Reconstructing quantum states with quantum reservoir networks. *IEEE Transactions on Neural Networks and Learning Systems*, 32(7):3148–3155, 2020.
- [49] Sanjib Ghosh, Kohei Nakajima, Tanjung Krisnanda, Keisuke Fujii, and Timothy CH Liew. Quantum neuromorphic computing with reservoir computing networks. *Advanced Quantum Technologies*, 4(9):2100053, 2021.
- [50] Xiao-Wei Zheng, Jun-Cong Zheng, Xue-Feng Pan, and Pengbo Li. Quantum-enhanced sensing of photonic modes with cat states. *arXiv preprint arXiv:2503.23531*, 2025.

- [51] Mazyar Mirrahimi, Zaki Leghtas, Victor V Albert, Steven Touzard, Robert J Schoelkopf, Liang Jiang, and Michel H Devoret. Dynamically protected cat-qubits: a new paradigm for universal quantum computation. *New Journal of Physics*, 16(4):045014, 2014.
- [52] Alexei Ourjoumtsev, Hyunseok Jeong, Rosa Tualle-Brouiri, and Philippe Grangier. Generation of optical ‘schrodinger cats’ from photon number states. *Nature*, 448(7155):784–786, 2007.
- [53] Gianluca Kosmella, Ripalta Stabile, and Jaron Sanders. Noise-resilient designs and analysis for optical neural networks. *Neuromorphic Computing and Engineering*, 4(4):044002, 2024.
- [54] Guangxin Liu, Wenjie Zhou, Dmitrii Gromyko, Ding Huang, Zhaogang Dong, Renming Liu, Juanfeng Zhu, Jingfeng Liu, Cheng-Wei Qiu, and Lin Wu. Single-photon generation and manipulation in quantum nanophotonics. *Applied Physics Reviews*, 12(1), 2025.
- [55] Marc-Antoine Lemonde, Nicolas Didier, and Aashish A Clerk. Antibunching and unconventional photon blockade with gaussian squeezed states. *Physical Review A*, 90(6):063824, 2014.
- [56] H Flayac and V Savona. Unconventional photon blockade. *Physical Review A*, 96(5):053810, 2017.
- [57] Vittorio Giovannetti, Seth Lloyd, and Lorenzo Maccone. Advances in quantum metrology. *Nature photonics*, 5(4):222–229, 2011.
- [58] Christian L Degen, Friedemann Reinhard, and Paola Cappellaro. Quantum sensing. *Reviews of modern physics*, 89(3):035002, 2017.
- [59] Stefano Pirandola, B Roy Bardhan, Tobias Gehring, Christian Weedbrook, and Seth Lloyd. Advances in photonic quantum sensing. *Nature Photonics*, 12(12):724–733, 2018.
- [60] Emanuele Polino, Mauro Valeri, Nicolò Spagnolo, and Fabio Sciarrino. Photonic quantum metrology. *AVS Quantum Science*, 2(2), 2020.
- [61] Saeed A Khan, Sridhar Prabhu, Logan G Wright, and Peter L McMahon. Quantum computational-sensing advantage. *arXiv preprint arXiv:2507.16918*, 2025.
- [62] Boris Kantsepolsky, Itzhak Aviv, Roye Weitzfeld, and Eliyahu Bordo. Exploring quantum sensing potential for systems applications. *IEEE Access*, 11:31569–31582, 2023.
- [63] Maggie Tse, Haocun Yu, Nutsinee Kijbunchoo, A Fernandez-Galiana, P Dupej, L Barsotti, CD Blair, DD Brown, SE ea Dwyer, A Effler, et al. Quantum-enhanced advanced ligo detectors in the era of gravitational-wave astronomy. *Physical Review Letters*, 123(23):231107, 2019.
- [64] Nabeel Aslam, Hengyun Zhou, Elana K Urbach, Matthew J Turner, Ronald L Walsworth, Mikhail D Lukin, and Hongkun Park. Quantum sensors for biomedical applications. *Nature Reviews Physics*, 5(3):157–169, 2023.
- [65] Anatoliy A Kosterev and Frank K Tittel. Chemical sensors based on quantum cascade lasers. *IEEE journal of quantum electronics*, 38(6):582–591, 2002.
- [66] Min Yu, Yu Liu, Pengcheng Yang, Musang Gong, Qingyun Cao, Shaoliang Zhang, Haibin Liu, Markus Heyl, Tomoki Ozawa, Nathan Goldman, et al. Quantum fisher information measurement and verification of the quantum cramer–rao bound in a solid-state qubit. *npj Quantum Information*, 8(1):56, 2022.
- [67] Jing Liu, Mao Zhang, Hongzhen Chen, Lingna Wang, and Haidong Yuan. Optimal scheme for quantum metrology. *Advanced Quantum Technologies*, 5(1):2100080, 2022.
- [68] Lukas J. Fiderer, Jonas Schuff, and Daniel Braun. Neural-network heuristics for adaptive bayesian quantum estimation. *PRX Quantum*, 2:020303, Apr 2021.
- [69] Alessio Fallani, Matteo A. C. Rossi, Dario Tamascelli, and Marco G. Genoni. Learning feedback control strategies for quantum metrology. *PRX Quantum*, 3:020310, Apr 2022.

- [70] Luca Pezzè. Machine learning for optical quantum metrology. *Advanced Photonics*, 5(2):020501, 2023.
- [71] A Muñoz de las Heras, Cristian Tabares, Jan T Schneider, Luca Tagliacozzo, Diego Porras, and A González-Tudela. Photonic quantum metrology with variational quantum optical nonlinearities. *Physical Review Research*, 6(1):013299, 2024.
- [72] Steven M Kay. *Fundamentals of statistical signal processing: estimation theory*. Prentice-Hall, Inc., 1993.
- [73] Martin Larocca, Supanut Thanasilp, Samson Wang, Kunal Sharma, Jacob Biamonte, Patrick J Coles, Lukasz Cincio, Jarrod R McClean, Zoë Holmes, and Marco Cerezo. Barren plateaus in variational quantum computing. *Nature Reviews Physics*, pages 1–16, 2025.
- [74] Stanisław Świerczewski, Wouter Verstraelen, Piotr Deuar, Barbara Pietka, Timothy CH Liew, Michał Matuszewski, and Andrzej Opala. Phase-space framework for noisy intermediate-scale quantum optical neural networks. *arXiv preprint arXiv:2507.07684*, 2025.
- [75] Piotr Deuar, Alex Ferrier, Michał Matuszewski, Giuliano Orso, and Marzena H Szymańska. Fully quantum scalable description of driven-dissipative lattice models. *PRX Quantum*, 2(1):010319, 2021.
- [76] I Tikhonenkov, JR Anglin, and A Vardi. Quantum dynamics of bose-hubbard hamiltonians beyond the hartree-fock-bogoliubov approximation: The bogoliubov back-reaction approximation. *Physical Review A—Atomic, Molecular, and Optical Physics*, 75(1):013613, 2007.
- [77] Mathias Van Regemortel, Wim Casteels, Iacopo Carusotto, and Michiel Wouters. Spontaneous beliaev-landau scattering out of equilibrium. *Physical Review A*, 96(5):053854, 2017.